DESIGN OF ASYMMETRIC REFLECTIVE SEMICONDUCTOR OPTICAL AMPLIFIER IN WAVELENGTH DIVISION MULTIPLEXING PASSIVE OPTICAL NETWORKS

DESIGN OF ASYMMETRIC REFLECTIVE SEMICONDUCTOR OPTICAL AMPLIFIER IN WAVELENGTH DIVISION MULTIPLEXING PASSIVE OPTICAL NETWORKS

BY

YUNFEI CAI, B.Eng.

A THESIS

SUBMITTED TO THE DEPARTMENT OF ELECTRICAL & COMPUTER ENGINEERING

AND THE SCHOOL OF GRADUATE STUDIES

OF MCMASTER UNIVERSITY

IN PARTIAL FULFILMENT OF THE REQUIREMENTS

FOR THE DEGREE OF

MASTER OF APPLIED SCIENCE

Master of Applied Science (2013) McMaster University

(Electrical & Computer Engineering) Hamilton, Ontario, Canada

TITLE: DESIGN OF ASYMMETRIC REFLECTIVE SEMICONDUCTOR OPTICAL AMPLIFIER IN WAVELENGTH DIVISION MULTIPLEXING PASSIVE OPTICAL NETWORKS

AUTHOR: YUNFEI CAI

B.Eng., (Electrical Engineering)

Wuhan University, Wuhan, China

SUPERVISOR: Dr. Xun Li

NUMBER OF PAGES: xvii, 63

To my parents

Abstract

Reflective semiconductor optical amplifiers (RSOA) are widely used in wavelength-division-multiplexed passive optical networks (WDM-PON). RSOAs in optical network units (ONUs) are operated in the gain saturation region so that the amplitude squeezing effect can be used to erase the information on downstream signals, however, the upstream signals go through the same RSOA need to be amplified.

In order to use one RSOA to satisfy the need of erasing the information on downstream signal by using amplitude squeezing effect and amplifying the upstream signal at the same time, an asymmetric RSOA design is proposed and demonstrated in this thesis. The ridge width becomes narrower along the traveling direction of the downstream signal so that the downstream signal can be amplified in the saturation region of the RSOA. At the same time, the ridge width increases in the traveling direction of the upstream signal, so that the modulated upstream signal can be amplified by the asymmetric RSOA. In this thesis, I mainly focus on the designing of the structure of the RSOA to enlarge the gain difference between upstream and downstream gain. Difference between wide end and narrow end effective indices, cavity length, the way that effective index changes from the wide end to the narrow end and bias current are factors that can affect the gain difference. How the device performance is affected by the factors were analyzed. An optimized structure of asymmetric RSOA is then

proposed according to the effects of the factors. The performance of the asymmetric RSOA, including gain dynamic performance, saturation output power, and upstream output power, is compared with symmetric RSOA. The asymmetric RSOA shows better performance in erasing the downstream signal information as well as amplifying upstream signal.

Acknowledgements

I would like to take this chance to thank all the people who love me and support me. First of all, I would like to sincerely thank my supervisor Dr. Xun Li for his great vision and remarkable help. This thesis would not have been possible without his help. He gave guidance and support for all aspects in my life in my graduate study process. I respect him not only as an excellent professor but also as a great person.

I would also like to show my gratitude to Dr. Shiva Kumar, Dr. Wei-Ping Huang and Dr. J.K. Zhang for their excellent lectures on fiber-optical communication system, waveguide and digital communication topics. They show me professionalism in academic as well as good attitude in life.

I am very grateful to Haibo Liang for his helpful discussions with me. Yefeng Wen has always been a good listener and advisor for me. Thank Shuo Shao for his spiritual support and encouragement. I would like to thank all of my friends in McMaster University for sharing their life in these two years with me.

I acknowledge the ECE administrative and technical support. I would like to give special thanks to dear Ms.Cheryl Gies for being so helpful and caring to me. Thank Ms.Kelly Lyth, Ms.Danielle Marcellin, Mr.Tyler Ackland, Mr.Chris Fulton, Mr.Dan Anthony Manolescu, Mr.Steve Spencer for their efficient work.

Last but not least, I would like to give special thanks to my parents - for all these

years of love, sacrifice and support. Thanks for supporting my decisions and giving me freedom to do what I want to do. You are the reasons of my life.

Notation and abbreviations

COs	central offices
PONs	passive optical networks
OLT	optical line terminal
ONU	optical network unit
IP	internet protocol
WDM	wavelength-division multiplexing
P2P	point-to-point
CWDM	coarse WDM
DWDM	dense WDM
AWG	arrayed waveguide grating
FSR	free spectral range
P2MP	point-to-multi-point
TX	transmitter
RX	receiver
ASE	amplified spontaneous emission
FP-LD	Fabry-Perot laser diode
RSOA	reflective semiconductor optical amplifier

SOA	semiconductor optical amplifier
CW	continuous wave
FP-SOA	Fabry-Perot SOA
TW-SOA	traveling-wave SOA
MQW	multi-quantum well
$\vec{E}$	electric field
$\vec{H}$	magnetic field
$\vec{r}$	space coordinate vector
$\vec{D}$	electric flux density
$\vec{B}$	magnetic flux density
$\vec{J}$	current density
ρ	charge density
ε	time domain permittivity of the medium
μ_0	permeability in vacuum
ε_0	permittivity in vacuum
χ	dimensionless time domain susceptibility of the medium
c	speed of light in vacuum
$\vec{u}$	frequency domain responses of the slow-varying harmonic wave envelope function
$\vec{x}$	unit vector along x direction
$\phi(x, y)$	cross-sectional field distribution
$e(z, t)$	longitudinal slow-varying field envelope function
ω_k	kth channel carrier signal angular frequency
α_s	modal loss
α_m	linewidth enhancement factor

v_g	group velocity
$\widetilde{s}$	spontaneous emission contribution
n_{eff}	dimensionless effective index
$\overline{s}$	time averaged spontaneous emission
γ	dimensionless coupling coefficient of the spontaneous emission
$\delta()$	Dirac function
$\hbar$	reduced Planck's constant
λ_k	corresponding wavelength to ω_k
a_1	gain coefficient
λ_0	peak wavelength at transparency
κ_0	constant characterizing the gain-peak shift
r_1	field reflectivity at the left (anti-reflective) facet
r_2	field reflectivity at the right (reflective) facet
P_{out1}	output power at left (anti-reflective) facet
P_{out2}	output power at right (reflective) facet
R_1	power reflectivity at the left (anti-reflective) facet
R_2	power reflectivity at the right (reflective) facet
LSHB	longitudinal spatial hole burning
$N(z,t)$	carrier density
J	injection current density
η	injection efficiency
A	minority carrier Shockley-Read-Hall (SRH) coefficient
B	spontaneous emission coefficient
C	Auger recombination coefficient

Γ	confinement factor
d	active region thickness
$\sum_{ar}$	cross-sectional area of the active region
SCH	separated confinement heterostructure
e_f	forward propagation field
e_r	backward propagation field

Contents

List of Figures

Chapter 1

Introduction

1.1 Background of the Research

1.1.1 Wavelength-Division-Multiplexed Passive Optical Network (WDM-PON)

The access network, also known as the "last kilometer" network, connects the service provider central offices (COs) to businesses and residential subscribers. The bandwidth demand in the access network has been increasing rapidly. Passive optical networks (PONs) have evolved to provide much higher bandwidth in the access network. A PON is a point-to-multipoint optical network, where an optical line terminal (OLT) at the CO is connected to many optical network units (ONUs) at remote nodes through one or multiple 1:N optical splitters. The network between the OLT and the ONU is passive, i.e. it does not require any power supply. Many telecom operators are considering to deploy PONs using a fiber-to-the-x (FTTx) model (where x = building (B), curb (C), home (H), premises (P), etc.) to support converged Internet protocol

(IP) video, voice, and data services. Although the PON provides higher bandwidth than traditional copper-based access networks, there exists the need for further increasing the bandwidth of the PON by employing wavelength-division multiplexing (WDM) so that multiple wavelengths may be supported in either or both upstream and downstream directions. Such a PON is known as a WDM-PON [Amitabha Banerjee,Youngil Park, et al., 2005]. WDM-PON is an attractive solution for broadband access networks for three reasons. First, they allow the same fiber infrastructure to be shared by different sets of wavelengths; second, they eliminate the need for time-mutiplexing and ranging protocols; third, they provide virtual point-to-point (P2P) connections with data transparency and a high degree of data security and independence [P. Healey, P. Townsend, C. Ford, L. Johnston, P. Townley, I. Lealman, L. Rivers, S. Perrin and R. Moore, 2001]. WDM-PON can be divided into coarse WDM-PON and dense WDM-PON. Wavelength spacing of more than 20 nm is generally called coarse WDM(CWDM). Dense WDM (DWDM) has wavelength spacing that is far lesser than that of CWDM, typically less than 3.2 nm. A DWDM-PON is expected to be very useful for providing enough bandwidth to many subscribers, and it is regarded as the ultimate PON system [Amitabha Banerjee,Youngil Park, et al., 2005]. However, WDM-PONs can be relatively expensive to implement due to the cost of the specified wavelength sources at both OLTs and ONUs. There is also an optional cost penalty associated with managing a broad range of wavelengths. A typical WDM-PON architecture comprises a CO, two cyclic arrayed waveguide gratings (AWGs), a trunk or feeder fiber, a series of distribution fibers, and ONUs at the subscriber premises, as illustrated in figure 1.1 [E. Wong, 2012].

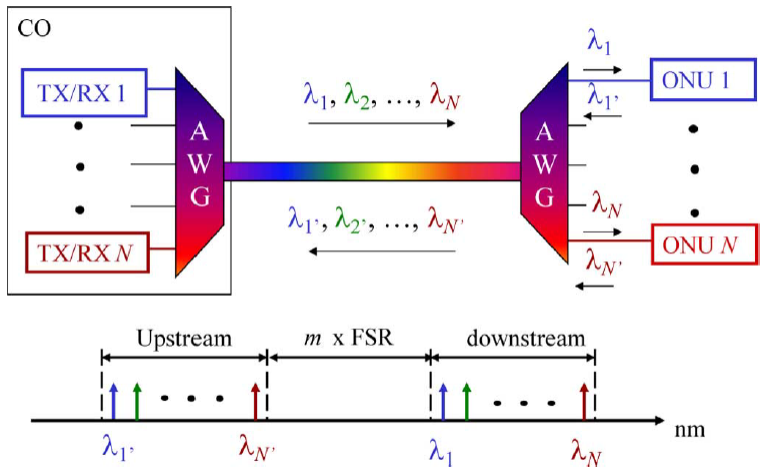

Figure 1.1: Architecture of a WDM-PON.

The first AWG located at the CO multiplexes downstream wavelengths to the ONUs and demultiplexes upstream wavelengths from the ONUs. The trunk fiber carries the multiplexed downstream wavelengths to a second cyclic AWG located at a remote node. The second AWG demultiplexes the downstream wavelengths and directs each into a distribution fiber for transmission to the ONUs. The downstream and upstream wavelengths allocated to each ONU are intentionally spaced at a multiple of the free spectral range (FSR) of the AWG, allowing both wavelengths to be directed in and out of the same AWG port that is connected to the destination ONU. In figure 1.1, the downstream wavelengths destined for ONU 1, ONU 2,..., and ONU N, are denoted λ_1, λ_2, ..., and λ_N respectively. Likewise, upstream wavelengths from ONU 1, ONU 2, ..., and ONU N, that are destined for the CO are denoted λ'_1, λ'_2, ..., and λ'_N, respectively. Although a WDM PON has a physical point-to-multi-point (P2MP) topology, logical P2P connections are facilitated between the CO and each

ONU. In the example shown in figure 1.1, ONU N receives downstream signals on λ_N and transmits upstream signals on λ'_N. The capacity on these wavelengths is solely dedicated to that ONU [E. Wong, 2012].

1.1.2 Reflective Semiconductor Optical Amplifier in WDM-PON Systems

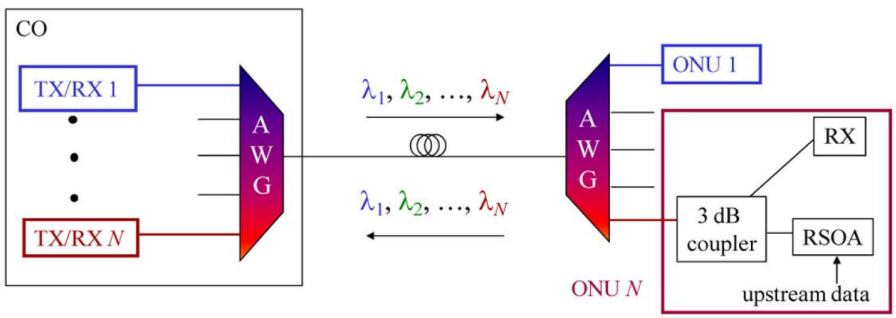

Figure 1.2: Architecture of WDM-PON showing colorless sources based on wavelength reuse scheme.

In wavelength reuse schemes the optical source is not used in the ONU. Downstream wavelengths are remodulated with upstream data, and then upstream signals are sent towards the CO. Figure 1.2 describes a WDM-PON that uses the wavelength reuse scheme. In figure 1.2 TX denotes transmitter, RX denotes receiver, ASE spectrum denotes amplified spontaneous emission spectrum. Except for carrying downstream signals, the downstream wavelength is also used to seed an reflective semiconductor optical amplifier (RSOA) located at the designated ONU. All RSOAs are operated in the gain saturation region so that the amplitude squeezing effect can be used to erase

the information on downstream signals [Y. Katagiri, K. Suzuki, and K. Aidai, 1999, Y.-L. Hsueh, M. S. Rogge, S. Yamamoto, and L. G. Kazovsky, 2005]. The amplified RSOAs output have the same wavelengths as the downstream wavelengths and can be directly modulated with upstream signals. Therefore, as shown in figure 1.2, the downstream and upstream wavelengths of an ONU are identical [E. Wong, 2012]. The merit of the wavelength reuse scheme is the remodulation of the downstream wavelength channel, thus eliminating the need for seeding sources, is not as costly as using tunable lasers. In another kind of colorless sources, optical light emitted from the CO is fed into the ONUs to injection- lock Fabry-Perot laser diodes (FP-LDs) [D. J. Shin, D. K. Jung, et al., 2003, K. Y. Cho, Y. Takushima, and Y. C. Chung, 2010c, KIM, H.D., KANG, S.-G., and LEE, C.-H., 2000] or to RSOAs [M. D. Feuer, J. M.Wiesenfeld,et al., 1996, P. Healey, P. Townsend, C. Ford, L. Johnston, P. Townley, I. Lealman, L. Rivers, S. Perrin and R. Moore, 2001]. As shown in figure 1.3, the injection- locking or wavelength seeding light may be equipped by spectral slicing light from a centralized broadband light source in the CO.

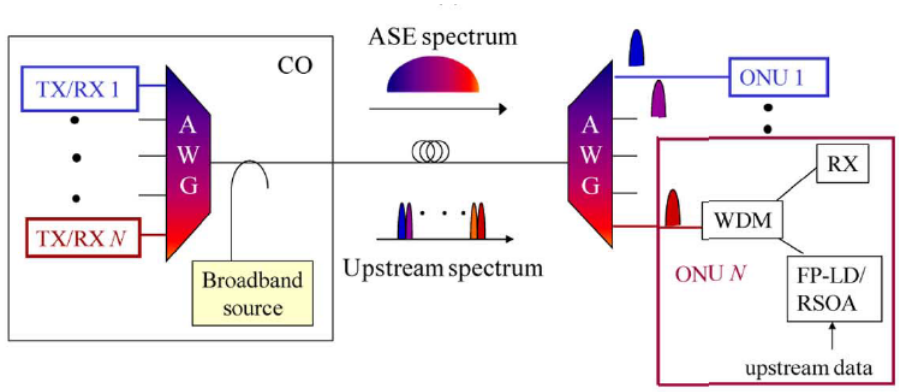

Figure 1.3: Architecture of WDM-PON showing colorless sources based on injection-locking/wavelength-seeded scheme.

Aside from using an RSOA to amplify and modulate the input signal, the wavelength seeding scheme is identical to the injection-locking scheme. All ONUs may be furnished with identical FP-LDs or RSOAs, as the transmitting wavelength of a colorless ONU is determined by the wavelength of the input light. Nevertheless, the above schemes require utilizing additional broadband light source(s) and their transmission performance is affected by fiber dispersion, Rayleigh backscattering noise, and ASE noise from the broadband light source and the colorless source. Further more, the modulation bandwidth of the colorless source is limiting upstream transmission bit rate. In order to provide higher transmission bit rates, proposals which utilizing multi-level narrow bandwidth modulation formats [K. Y. Cho, Y. Takushima, and Y. C. Chung, 2010b, M. Omella,V. Polo, et al., 2008], electronic equalization [K. Y. Cho, Y. Takushima, and Y. C. Chung, 2010a,c, K.Y.Cho, Y.Takushima, Y.C.Chung, 2008], and optical equalization [H. Kim, 2011, Lirong Huang, Wei Hong and Guiying Jiang, 2013] have been proved effective in wavelength seeding of RSOA at 10 Gb/s operation.

E.Wong proposed self-seeding scheme in [E. Wong, K. Lee, and T. B. Anderson, 2007], spectral slicing continuous wave (CW) light is self-seeding its own RSOA in each ONU. As shown in figure 1.4, the AWG implemented in the remote node spectrally slices ASE light emitted from each RSOA. λ'_1, λ'_2, ..., and λ'_N in figure 1.4 indicate the upstream self-seeding wavelengths whereas the downstream wavelengths are represented by λ_1, λ_2, ..., and λ_N .

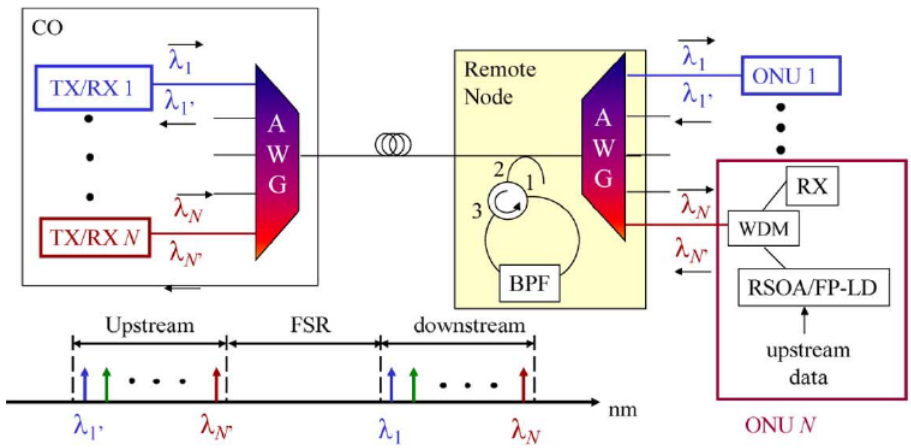

Figure 1.4: Architecture of WDM-PON showing colorless sources based on self-seeding scheme.

A passive reflective path includes an optical circulator and a bandpass filter (BPF) with a passband comparable to the FSR of the AWG is used so that each RSOA will be self-seeded by only one spectral slicing light. Self-seeding eliminates the need for active temperature tracking in remote nodes. More over, identical RSOAs can be implemented at all ONUs since the input and output wavelength of each RSOA is only dependant on the spectral characteristics of the AWG and BPF. A disadvantage of this scheme is that due to non-zero polarization dependent gain of the RSOAs, the self-seeding scheme is polarization dependent. The solution to the problem is proposed by Presi in [M. Presi and E. Ciaramella, 2011]. By using a Faraday rotator mirror in the feedback path to reflect light back to the RSOA with an orthogonal state of polarization and hence alleviate polarization dependency.

1.2 Research Motivation

As we can see in subsection 1.1.2, RSOAs are widely used in colorless sources in different categories of WDM-PON schemes. The main advantage of using a RSOA is that the incoming downstream signal can be reflected at the reflective facet of RSOA and hence become upstream signal of the same wavelength. In this way, light source(s) can be eliminated all together in ONU and thus the optical source in the ONU becomes colorless. Colorless ONU device is able to be used in any wavelength channels, enabling us to produce them massively and achieve significant cost reduction [Hiroki Takesue, Toshihiko Sugie, 2002, 2003]. As the cost of ONU device has a direct impact on the cost per customer and in general on the overall cost of the access network [J Prat, PE Balaguer, JM Gene, O Diaz, S Figuerola, 2002], using RSOA in cost effective colorless optical sources can help us to overcome the cost obstacle in fulfilling FTTH concept. RSOAs in optical network units (ONUs) are operated in the gain saturation region so that the amplitude squeezing effect can be used to erase the information on downstream signals [Y. Katagiri, K. Suzuki, and K. Aidai, 1999], however, the upstream signals go through the same RSOA need to be amplified. In order to use one RSOA to satisfy the need of erasing the information on downstream signal by using amplitude squeezing effect and amplifying the upstream signal at the same time, an asymmetric RSOA design is proposed and demonstrated in this thesis. The ridge width becomes narrower along the traveling direction of the downstream signal the downstream signal can be amplified in the saturation region of the asymmetric RSOA, at the same time, the ridge width increases in the traveling direction of the upstream signal, so that the modulated upstream signal can be amplified by the asymmetric RSOA.

1.3 Outline of the Thesis

After describing the principle of the asymmetric RSOA in Chapter 2, the detailed numerical model is presented in Chapter 3. In Chapter 4, the performance of the proposed asymmetric RSOA is demonstrated and discussed. A conclusion is drawn in Chapter 5.

1.4 Main Contribution of the Thesis

This thesis focused on the design of asymmetric RSOA in wavelength division multiplexing passive optical networks. We proposed the structure of asymmetric reflective semiconductor optical amplifier and its application in wavelength division multiplexing passive optical networks. We studied the performance of asymmetric reflective semiconductor optical amplifier in wavelength division multiplexing passive optical networks.

Chapter 2

Principle of Asymmetric Reflective Semiconductor Optical Amplifier

2.1 Introduction

In this chapter, the principles underlying asymmetric RSOA design are reviewed. First, several characters of semiconductor optical amplifiers (SOA), including small-signal gain, gain saturation, gain dynamic effects are explained and discussed later in simulation results in Chapter 4. Then asymmetric RSOA structure is chosen to accentuate the particular characteristic desirable for our application of using it to erase the information of downstream signal as well as amplify the upstream signal.

2.2 Basic Description of Semiconductor Optical Amplifiers

An SOA is an optoelectronic device which under suitable operating conditions can amplify an input signal [Michael J. Connelly, 2002]. Figure 2.1 illustrates a basic SOA.

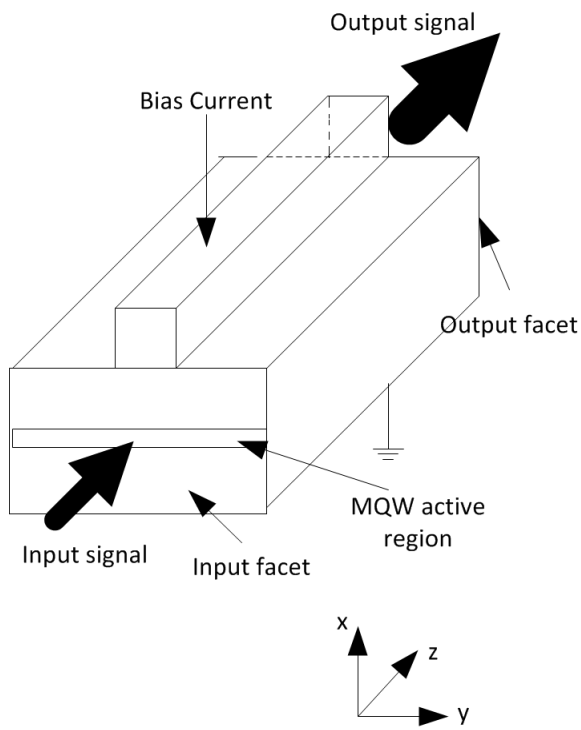

Figure 2.1: Structural diagram of a basic SOA.

As we can see in Figure 2.1, bias current serves as an electrical pump source for the SOA. A ridge waveguide is used to confine signal propagation in the active region. The amplifier facets are equipped with anti-reflective or reflective coatings according to utilization. An SOA with significant reflections on both facets is called Fabry-Perot

SOA (FP-SOA). In a FP-SOA the signal undergoes many passes through the cavity. If the reflections on both facets are negligible, the SOA is called traveling-wave SOA (TW-SOA) [M. J. Connelly, 2001, Michael J. Connelly, 2002]. In this kind of SOA, signal only goes a single pass in the cavity. A RSOA has one facet with significant reflection and the other has negligible reflection.

Small-Signal Gain and Gain Bandwidth

There are two different gain definitions for SOAs. The first is the intrinsic gain of the SOA, which is the ratio of the output signal power at the output facet to the input signal power at the input facet. The second definition is the fiber-to-fiber gain where coupling losses at input and output facets are considered [Michael J. Connelly, 2002]. These gains are usually expressed in dB unit. The gain we discuss in this thesis is the intrinsic gain.

Gain Saturation

The gain of an SOA is affected by the input signal power and internal noise generated by the amplification process. Gain is achieved in a SOA due to population inversion. The inversion level of a SOA is primarily set by the electrical pumping from the bias current. As the signal power increases, the carriers in the active region become depleted and the inversion level reduces leading to a decrease in the amplifier gain. This effect is known as gain saturation as the signal level increases, the amplifier saturates and cannot produce any more output power, and therefore the gain reduces. Gain saturation can cause significant signal distortion. A typical SOA gain changes with output signal power characteristic is shown in Figure 2.2. A useful parameter

for quantifying gain saturation is the saturation output power which is defined as the amplifier output signal power at which the amplifier gain is half the small-signal gain.

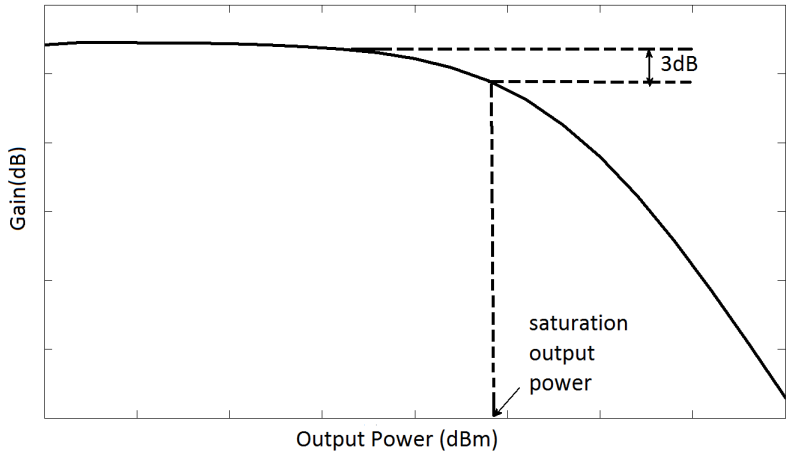

Figure 2.2: Typical SOA gain changes with output signal power characteristic.

Gain Dynamic Effects

One common application of SOAs is to be used to amplify modulated signals. In our case, SOA is used to amplify the modulated upstream signal in ONUs of WDM-PON. In SOAs the gain dynamic effects are determined by the carrier recombination lifetime which is typically of a few hundred picoseconds. This means that the amplifier gain will react relatively quickly to changes in the input signal power and can cause signal distortion.

2.3 Structure and Working Principle of Asymmetric Semiconductor Optical Amplifier

In this work, a multi-quantum well (MQW) structure was assumed. Comparing with bulk material MQW has many advantages, including lower transparency current, reduced temperature dependence on bias current and improved dynamic characters [A. Yariv, 1988, J. Piprek, J. K.White, and A. J. SpringThorpe, 2002, L. C. Chiu and A. Yariv, 1985, N. Holonyak, Jr., R. M. Kolbas, R. D. Dupuis, and P. D. Dapkus, 1980]. Ridge structure is essential to the design of asymmetric RSOA.

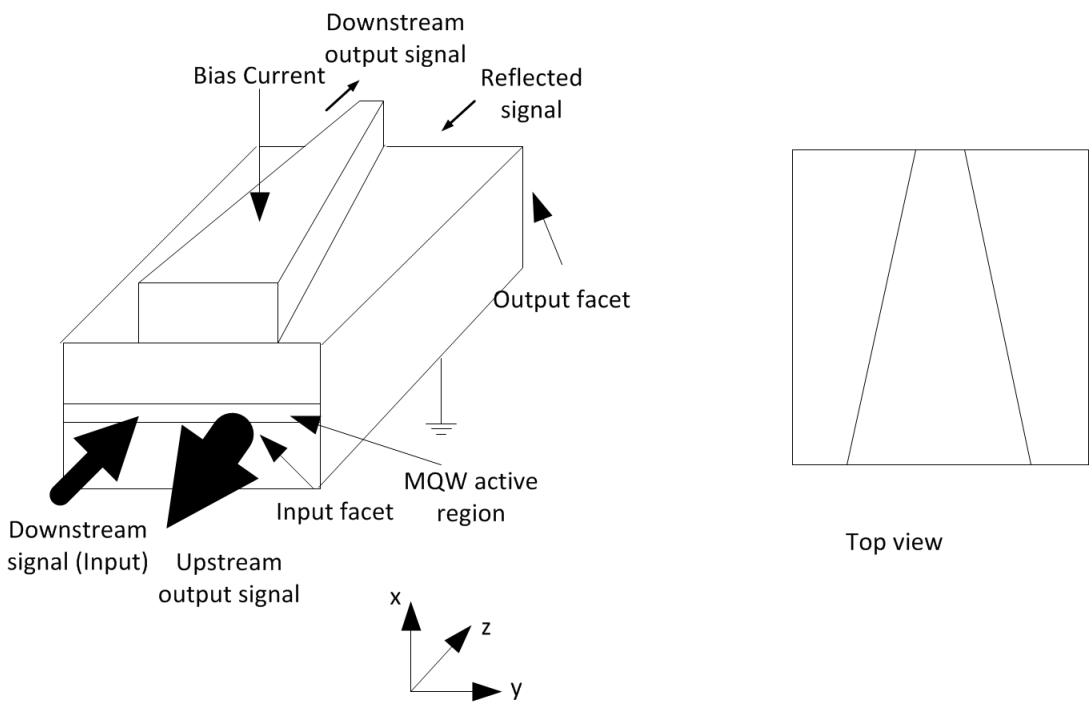

Figure 2.3: Structure of asymmetric RSOA.

As illustrated in figure 2.3, a ridge is etched longitudinally along the cavity, providing a closed circuit only through a small lateral region, hence enhance current confinement [W. Streifer and Burnham, 1978]. The ridge is achieved by introducing an additional layer through one cladding region which serves as an etch-stop during the etching process; a simple mask is used to define the lateral ridge structure [Scott B. Kuntze, 2009]. The other advantage of ridge is that it provides refractive index contrast to the optical mode and helps guiding optical wave propagation longitudinally [T. L. Paoli, 1977]. As we can see in figure 2.4, by changing the width of the ridge, the distribution of field, as well as, the confinement of optical wave in the cavity and the effective index of the waveguide alternate accordingly.

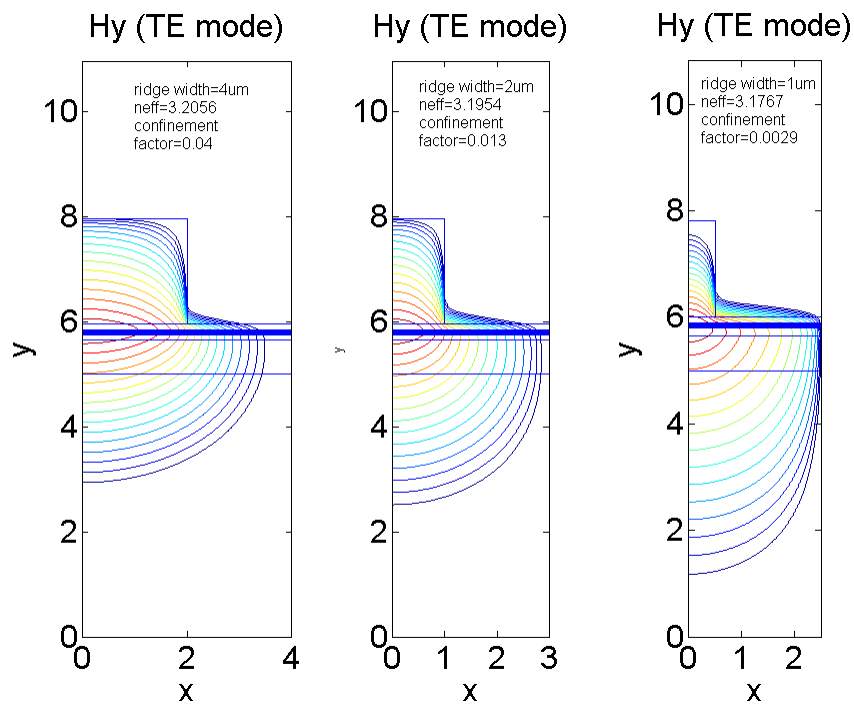

Figure 2.4: Hy field distribution changes with ridge width.

In our case, gain becomes smaller as the ridge width narrows down along the longitudinal direction of the cavity. Downstream signal comes in from the wide end of the cavity will be amplified by gradually reducing gain along the propagation direction, thus the amplitude squeezing effect can erase the information on downstream signals, at the same time, the ridge width increases in the traveling direction of the upstream signal, so that the modulated upstream signal can be amplified by the asymmetric RSOA.

2.4 Summary

In this chapter, the principles underlying asymmetric RSOA design are reviewed. The gain definition used in this thesis is explained. Output saturation power is defined and is going to be used in Chapter 4 for gain saturation performance discussion of this RSOA. The structure and working principle for the asymmetric RSOA are explained in section 2.3 in the application of using it to erase the information of downstream signal as well as amplify the upstream signal.

Chapter 3

Simulation Model of Asymmetric Reflective Semiconductor Optical Amplifier

3.1 Introduction

Computer aided modeling and simulation is a powerful approach for researching the underlying physics and steady-state and dynamic behaviors of asymmetric RSOA corresponding to a variety of design parameters. Models of asymmetric RSOA allow the designer to develop optimized devices. They also allow the designer to predict how an asymmetric RSOA behaves in a particular application. In this chapter, we concentrate on a specific quasi-2D model and the numerical analysis of it.

3.2 Optical Model

3.2.1 Longitudinal Direction Optical Equations

In this thesis, a broadband time-domain traveling wave model is utilized to perform a theoretical investigation of the proposed asymmetric RSOA. The governing equations are solved by wavelength slicing technique [J.W. Park, X. Li and W.P. Huang, 2003, Xun Li, 2009]. In this model, the electrical field propagation and reflection, the locally generated broadband spontaneous emission and amplification, carrier dynamics, gain dynamics and the multichannel optical signals are all included. The optical wave propagation along the longitudinal direction is governed by the K time-domain coupled partial differential equations [J. W. Park, 2004]:

$$\begin{aligned}\frac{1}{v_g}\frac{\partial e_{(f,r)}\left(z,t,\omega_k\right)}{\partial t} \pm \frac{\partial e_{(f,r)}\left(z,t,\omega_k\right)}{\partial z} \\ = \left\{-j\left(\beta\left(\omega_k\right)+\frac{1}{2}\Gamma(z)\alpha_m g\left(z,t,\omega_k\right)\right)+\frac{1}{2}\left(\Gamma(z)g\left(z,t,\omega_k\right)-\alpha_s\right)\right\} \\ \times e_{(f,r)}\left(z,t,\omega_k\right)+\tilde{s}_{(f,r)}\left(z,t,\omega_k\right)\end{aligned} \tag{3.1}$$

where $e_{(f,r)}$ are the forward and backward traveling electric fields. v_g is the group velocity in m/s. ω_k $(k = 1, 2, 3...K)$ is the angular frequency associated with subsection k, Γ is the confinement factor, unlike in symmetric RSOA, confinement factor in asymmetric RSOA changes along the longitudinal direction due to the change of the ridge width. So Γ needs to be calculated separately with the method explained in 3.2.3. Effective index n_{eff} in equations 3.3, 3.14 and 3.19 also has z dependency and needs to be treated separately as shown in 3.2.3. In equation 3.1, g is the material gain in $1/m$, α_s is the modal loss in $1/m$, and α_m denotes linewidth enhancement

factor. This model is called the full-wave model in [J. W. Park, 2004]. The phase information of both the signals and the noises are considered.

3.2.2 Boundary Conditions

The following boundary conditions are utilized at the ends of the RSOA.

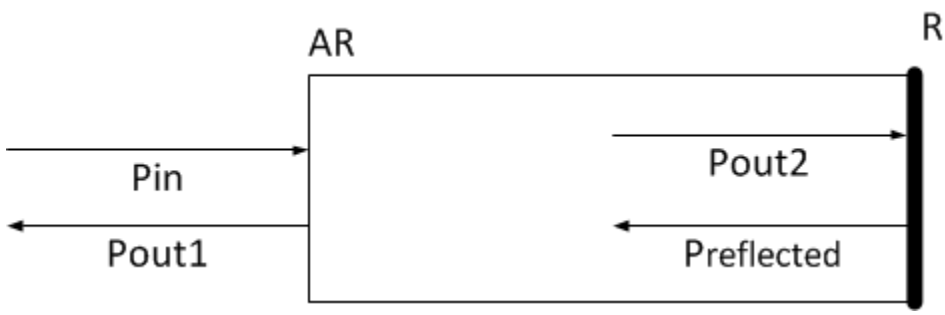

Figure 3.1: Structure of RSOA.

As illustrated in figure 3.1, the reflectivity of the left facet is suppressed by antireflection (AR) coating. The following boundary conditions are applied at the facets of the amplifier:

$$e_f\left(0,t,\omega_k\right) = (1-r_1)E_{in}\left(0,t,\omega_k\right) + r_1 e_r\left(0,t,\omega_k\right) \tag{3.2a}$$

$$e_r\left(L,t,\omega_k\right) = r_2 e_f\left(L,t,\omega_k\right) \tag{3.2b}$$

where r_1 is the field reflectivity at the left (anti-reflective) facet, r_2 is the field reflectivity at the right (reflective) facet. The output power of the kth channel from the SOA can be expressed as:

$$P_{out2} = \sum_{k=1}^{K} \frac{n_{eff}(L)\Gamma(L)}{2} \sqrt{\frac{\varepsilon_0}{\mu_0}} (1 - R_2) |e_f\,(L, t, \omega_k)\,|^2 \tag{3.3a}$$

$$P_{out1} = \sum_{k=1}^{K} \frac{n_{eff}(1)\Gamma(1)}{2} \sqrt{\frac{\varepsilon_0}{\mu_0}} (1 - R_1) |e_r\,(0, t, \omega_k)\,|^2 \tag{3.3b}$$

where P_{out1} and P_{out2} are the output power in W at left (anti-reflective) and right (reflective) facets. R_1 denotes the power reflectivity at the left (anti-reflective) facet, R_2 represents the power reflectivity at the right (reflective) facet. $R_{1,2}$ and $r_{1,2}$ have the relation $R_{1,2} = r_{1,2}^2$. The complex field calculated through equation 3.1 fluctuates in time, as the calculation result is affected by the random noise generator. Therefore, the output power can only be obtained by taking average of output power over a time period after the steady state is reached.

3.2.3 Cross-Sectional Governing Equations

In asymmetric RSOA, ridge width changes along longitudinal direction of device cavity, thus every spatial subsection has different cross-sectional structure, as well as, different confinement factor and different effective index. So the confinement factor and effective index cannot be set as constant coefficients for the whole cavity as we often do in the simulation of symmetric RSOA. In asymmetric RSOA simulation, confinement factor and effective index need to be solved separately in the cross-sectional structure and plugged in longitudinal optical equation 3.1 to reflect the structural change along the longitudinal direction of the device. The demonstration of simulation of confinement factor and effective index in the cross-sectional structure of asymmetric RSOA is shown in the section.

The Maxwell equations for the source free region are like:

$$\nabla \times \vec{E} = -\frac{\partial}{\partial t}\vec{B} = -j\omega\mu\vec{H}, \tag{3.4}$$

$$\nabla \times \vec{H} = \frac{\partial}{\partial t}\vec{D} = j\omega\varepsilon\vec{E}, \tag{3.5}$$

$$\nabla \cdot \vec{D} = 0, \tag{3.6}$$

$$\nabla \cdot \vec{B} = 0, \tag{3.7}$$

From equation 3.4 and equation 3.5 we can obtain:

$$\nabla \times \left(\frac{1}{\varepsilon}\nabla \times \vec{H}\right) - \omega^2\mu_0\vec{H} = 0; \tag{3.8}$$

where the material is assumed nonmagnetic, so $\mu = \mu_0$. By applying the divergence relation $\nabla \cdot \vec{H} = 0$, the longitudinal component H_z can be derived:

$$H_z = \frac{1}{j\beta}\left(\frac{\partial H_x}{\partial x} + \frac{\partial H_y}{\partial y}\right) \tag{3.9}$$

Plugging equation 3.9 into equation 3.8, we can eliminate H_z and use only H_x and H_y to express equation 3.8:

$$\frac{\partial^2 H_x}{\partial x^2} + \frac{\varepsilon_y \partial^2 H_x}{\varepsilon_z \partial y^2} + \left(1 - \frac{\varepsilon_y}{\varepsilon_z}\right)\frac{\partial^2 H_y}{\partial x \partial y} + k^2\varepsilon_y H_x = \beta^2 H_x, \tag{3.10a}$$

$$\frac{\partial^2 H_y}{\partial y^2} + \frac{\varepsilon_x \partial^2 H_y}{\varepsilon_z \partial x^2} + \left(1 - \frac{\varepsilon_x}{\varepsilon_z}\right)\frac{\partial^2 H_x}{\partial y \partial x} + k^2\varepsilon_x H_y = \beta^2 H_y \tag{3.10b}$$

where $k^2 \equiv \omega^2 \mu_0 \varepsilon_0$. With three known components of $\vec{H}$, $\vec{D}$ can be derived with the relation $\nabla \times \vec{H} = j\omega\vec{D}$:

$$\begin{aligned} D_x &= -\frac{1}{\omega\beta}\left(\frac{\partial^2 H_x}{\partial y \partial x} + \frac{\partial^2 H_y}{\partial y^2}\right) + \frac{\beta}{\omega} H_y, \\ D_y &= \frac{1}{\omega\beta}\left(\frac{\partial^2 H_y}{\partial x \partial y} + \frac{\partial^2 H_x}{\partial x^2}\right) - \frac{\beta}{\omega} H_x, \\ D_z &= \frac{j}{\omega}\left(\frac{\partial H_x}{\partial y} - \frac{\partial H_y}{\partial x}\right) \end{aligned} \tag{3.11}$$

and electrical field can thus be derived by using $\vec{E} = \varepsilon^{-1}\vec{D}$,

$$\begin{bmatrix} E_x \\ E_y \end{bmatrix} = \frac{1}{\varepsilon_0} \begin{bmatrix} \frac{D_x}{\varepsilon_x} \\ \frac{D_y}{\varepsilon_y} \end{bmatrix} \tag{3.12}$$

$$E_z = \frac{1}{\varepsilon_0 \varepsilon_z} D_z = \frac{j}{\omega \varepsilon_0 \varepsilon_z}\left(\frac{\partial H_x}{\partial y} - \frac{\partial H_y}{\partial x}\right) \tag{3.13}$$

By solving H_x and H_y from equation 3.10, we can get all the six electrical and magnetic components from the equations derived above [Arman B.Fallahkhair, Kai.S.Li, Thomas E.Murphy, 2008, M.S Stern, 1995]. By utilizing piecewise linear interpolation method,we only need to calculate the effective indices and confinement factors at the wide end, narrow end and several other points along the longitudinal direction to get the distribution of effective index and confinement factor of the given cross-sectional structure. The illustration of the cross-sectional structure design of the RSOA is shown in figure 3.2:

Graded doped P-InP n=3.17 h=1~3μm		λ_g=918.6nm w=0.02~4μm
SCH 1 InGaAsP	n=3.17~3.37 h=10nm~300nm	
Barrier X(4~8) $In_{0.751}Ga_{0.249}As_{0.539}P_{0.461}$	n=3.3721 h=8~10nm	λ_g=1250nm
Well X(4~8) $In_{0.788}Ga_{0.212}As_{0.797}P_{0.203}$	n=3.56 h=5nm	λ_g=1600nm
Barrier $In_{0.751}Ga_{0.249}As_{0.539}P_{0.461}$	n=3.3721 h=8~10nm	λ_g=1250nm
SCH 2 InGaAsP	n=3.17~3.37 h=10nm~300nm	
Buffer P-InP	n=3.17 h=650nm	λ_g=918.6nm

Figure 3.2: Cross-sectional structure of a RSOA.

Utilizing vector finite difference mode solver proposed by Fallahkhair et al in [Arman B.Fallahkhair, Kai.S.Li, Thomas E.Murphy, 2008], changes of effective refractive index and confinement factor with ridge width can be found respectively. Figure 3.3 and figure 3.4 are the illustrations of changes of effective refractive index and confinement factor with ridge width for one example structure.

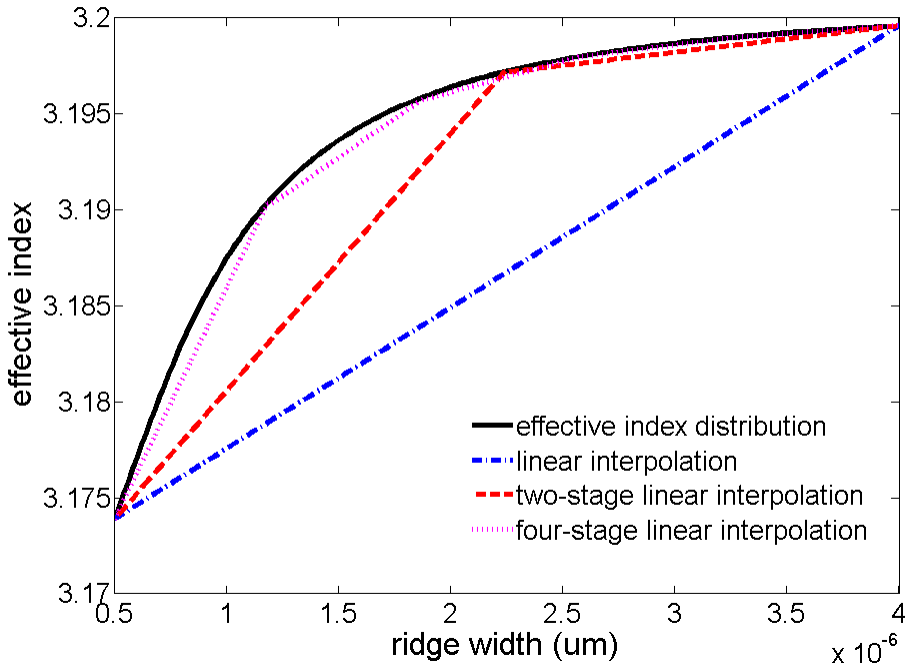

Figure 3.3: Effective index changes with the ridge width.

The comparison between effective index distribution calculated piece by piece along the longitudinal direction and linear interpolation is shown in figure 3.3. As we can see, one-stage linear interpolation can be a very effective approximation for the effective index distribution which means when we assume the effective index decreases linearly the ridge width can be considered as decreasing linearly as well. The average relative difference of one-stage linear interpolation is 0.24% and we only need to calculate the effective index at the wide and narrow ends to get the result. If further accuracy is needed for the simulation higher-stage linear interpolation can be applied. In the four-stage linear interpolation the average relative difference is 0.13%.

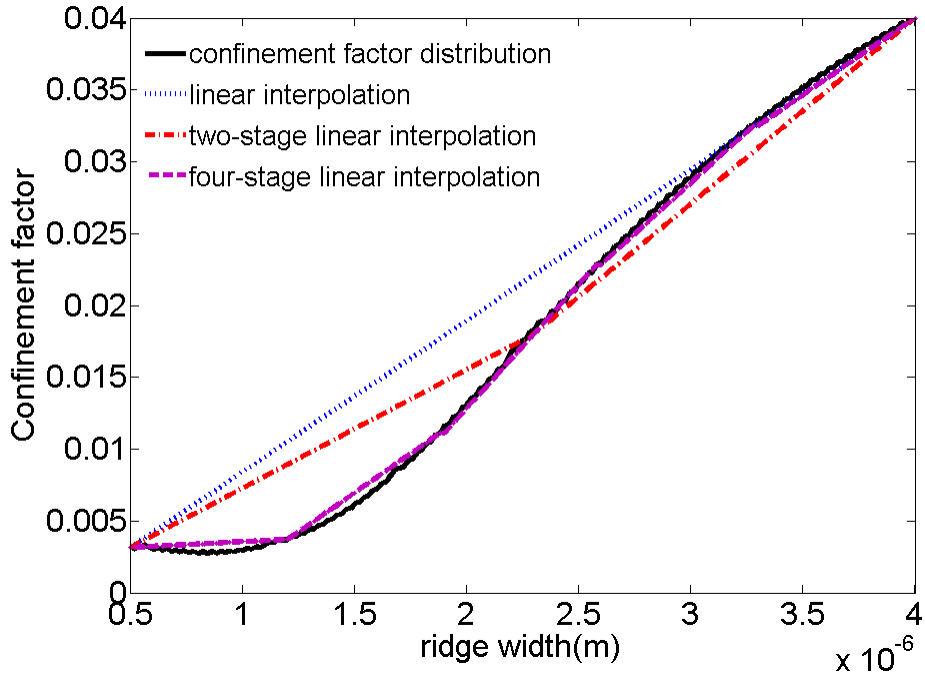

Figure 3.4: Confinement factor changes with ridge width.

The comparison between confinement factor distribution calculated piece by piece along the longitudinal direction and linear interpolation is shown in figure 3.4. The one-stage linear interpolation is not enough for the approximation of confinement factor distribution. The average relative difference is 53.5%. So higher-stage linear interpolation is needed. The average relative differences in two-stage,three-stage and four-stage linear interpolations are 38.6%, 14.9%, and 5% respectively. Without further notice, four-stage linear interpolation of confinement factor is applied for the later simulation results in the thesis.

3.2.4 Noise Treatment

The spontaneous emission noise $\widetilde{s}_{(f,r)}(z,t,\omega_k)$ is a Langevin noise source [C. H. Henry, 1986], therefore, the amplitude of the noise can be approximately modeled by the Gaussian distributed random process while the phase of the noise can be modeled by uniformly distributed random process [K. Vahala and A. Yariv, 1983a,b]. The Gaussian distributed random process has zero mean and the autocorrelation function is:

$$\langle|\widetilde{s}(z,t,\omega_k)||\widetilde{s}(z',t',\omega_k')|\rangle = 2\sqrt{\frac{\mu_0}{\varepsilon_0}}\frac{\gamma\Gamma(z)g_{sp}(z,t,\omega_k)\hbar\omega_k}{n_{eff}(z)}\delta(z-z')\delta(t-t')\delta(\omega_k-\omega_k'), \tag{3.14}$$

where γ is the dimensionless coupling coefficient of the spontaneous emission over the entire spatial sphere and spread over the entire frequency spectrum to the waveguide mode at the reference frequencies. The phenomenological coefficient γ must be introduced, unlike stimulated emission, photons produced in spontaneous emission go in every direction in a spatial sphere whereas the waveguide is built in one direction [Xun Li, 2009]. Therefore, only a certain percentage of photons produced by spontaneous emission can be captured by waveguide, this percentage is represented by γ [C. F. Janz and J. N. McMullin, 1995, M.Yamada, 1994]. Here, $\delta()$ denotes the Dirac function. g_{sp} is the spontaneous emission gain in $1/m$, and $\hbar$ is the reduced Planck's constant in Js.

3.3 Gain Model

The stimulated and spontaneous recombination mechanisms in [G. P. Agrawal and N. K. Dutt, 1993, S. L. Chuang, 1995] is taken as the principle for gain model in this

thesis. The MQW material gain is a function of E [Alan E. Willner, William Shieh, 1995, Dayan Ban and Edward H. Sargent, 2000, Mehdi Asghari, Ian H. White and Richard V. Penty, 1997], which expressed as

$$g(\omega) = \frac{\omega\rho_{2D}}{\varepsilon_0 nc}\int_{E_g^{mn}}^{\infty} dE\{|\mu(E)|^2[f_c^m(E) + f_v^n(E) - 1]\frac{\gamma_g\hbar}{(\gamma_g\hbar)^2 + (E-\hbar\omega)^2}\} \tag{3.15}$$

The QW structure spontaneous emission gain is given as

$$g_{sp}(\omega) = \frac{\omega\rho_{2D}}{\varepsilon_0 nc}\int_{E_g^{mn}}^{\infty} dE\{|\mu(E)|^2 f_c^m(E) f_v^n(E)\frac{\gamma_g\hbar}{(\gamma_g\hbar)^2 + (E-\hbar\omega)^2}\} \tag{3.16}$$

where ρ_{2D} is the $2D$ density of states in terms of transition energy E defined as

$$\rho_{2D} \equiv \frac{m_r}{\pi\hbar^2 L_z} \tag{3.17}$$

where L_z is the thickness of the QW. Here E_g^{mn} is bandgap energy in eV. $\mu(E)$ denotes dipole matrix in $C \cdot m$, γ_g is the phenomenological polariton factor. f_c^m and f_v^n are the quasi-Fermi distributions for the conduction band electrons and valence band holes, respectively. All the variables in equations 3.15 and 3.16 are defined in [Xun Li, 2009]. The material gain and spontaneous emission gain are updated at each step, varying from subsection to subsection discretized in the spectrum and varying from subsection to subsection along the longitudinal direction. The material gain profiles obtained according to the gain model is illustrated in figure 3.5

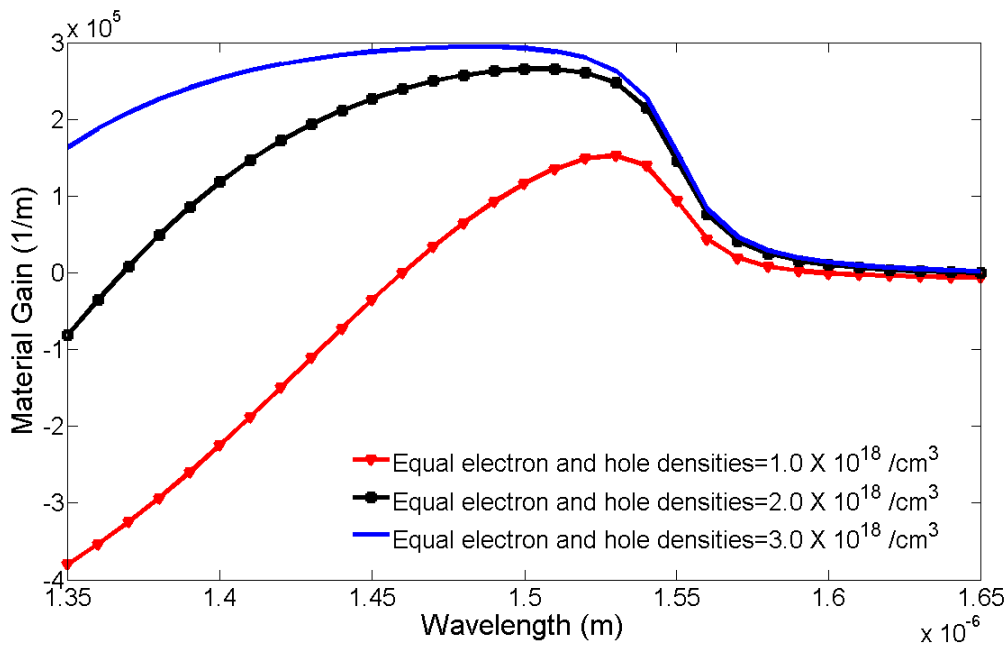

Figure 3.5: Material gain profiles.

3.4 The Carrier Rate Equation Model

The carrier distribution inside the active region is dictated by the distribution of optical wave intensity due to the longitudinal spatial hole burning (LSHB) [Xun Li, 2009]. If the carrier diffusion in the cross-sectional area, comparing to the carrier transport effect in longitudinal direction is negligible. Then carrier diffusion along (x,y) direction $\nabla^2_{(x,y)}N$ can be ignored. We only need a 1D model along the wave propagation direction to describe carrier density, i.e. carrier density N is a function of (z, t). Following energy conservation law, a carrier rate equation can be extracted phenomenologically through balancing carrier generation and recombination rates of time-dependent process. Carrier change rate $\triangle N$ should be equal to the difference

between total carrier generation rates and total carrier consumption rates [Xun Li, 2009]. Carriers are generated and can only be generated by current injection, and they can be consumed in stimulated emission, spontaneous emission and non-radiative recombination processes. Therefore, the following carrier rate equation can be obtained:

$$\frac{\partial N(z,t)}{\partial t} = \frac{\eta J(z,t)}{ed} - [AN(z,t) + BN^2(z,t) + CN^3(z,t)] - R_{stim}(z,t) \tag{3.18}$$

where $R_{stim}(m^3/s)$ is the stimulated emission rate given by:

$$R_{stim}(z,t) = \sum_{k=1}^{K} \frac{n_{eff}(z)}{2\hbar\omega_k} \sqrt{\frac{\epsilon_0}{\mu_0}} \frac{\Gamma(z)}{\sum_{ar}} g(z,\omega_k) \left| E_f(z,t,\omega_k) + E_r(z,t,\omega_k) \right|^2 \tag{3.19}$$

where N is the minority carrier density in $1/m^3$ inside the active region, J is the injection current density in A/m^2, η is the injection efficiency, $A(1/s)$, $B(m^3/s)$ and $C(m^6/s)$ are the minority carrier Shockley-Read-Hall (SRH), spontaneous emission, and Auger recombination coefficients, respectively. In addition, n_{eff} denotes the effective index of the guided optical mode, Γ denotes the confinement factor, d is the active region thickness in $1/m$, $\sum_{ar}$ represents the cross-sectional area of the active region in $1/m^2$, respectively, and $e_f(z,t,\omega_k)$ and $e_r(z,t,\omega_k)$ represent the forward and backward propagation field respectively. There are K different wavelengths elements in the propagation lightwave, so equations 3.18 and 3.19 have a summation of K equations. In equation 3.18, we do not distinguish electron and hole densities, as we have assumed a charge neutrality condition inside the active region [Alexei Sadovnikov, Xun Li, Wei-Ping Huang, 1995].

3.5 Implementation

Only one single stable mode is assumed in the optical waveguide of the device while the effective index and the confinement factor are obtained from solving optical field eigen value problem in the cross-section in subsection 3.2.3. Therefore, we only take the spacial dependence along the optical wave propagation direction into consideration. The finite difference method is applied to solve the partial differential equations 3.1.

Spatial and Spectral Discretization

As shown in figure 3.6, the RSOA structure is divided into N subsections so that LSHB effects can be taken into consideration. In the spectrum, the entire ASE spectrum from $1200nm$ to $1650nm$ (i.e. the full band) is uniformly sliced into K segments. It is crucial to consider the full noise bandwidth for the numerical computation as a narrow spectral range for the noise simulation in the optical amplifiers may lead to an underestimation of ASE introduced carrier depletion and gain saturation [J. W. Park, 2004, J.W. Park, X. Li and W.P. Huang, 2003].

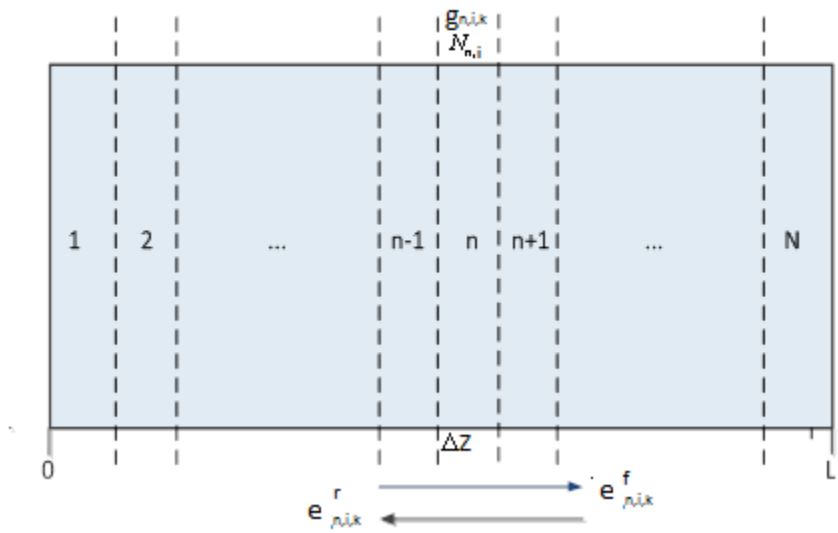

Figure 3.6: Schematic diagram of the device structure discretized in space into N subsections of equal length Δz.

As the bandwidth of each spectral slice in the ASE spectrum is inversely proportional to the number of slices (K) when the full band width is fixed. In the simulation we need to select a constant K as to achieve a proper balance between the simulation accuracy and efficiency. To reach such a balance and to obtain the converged simulation result the following simulation algorithm is developed as shown in figure 3.7

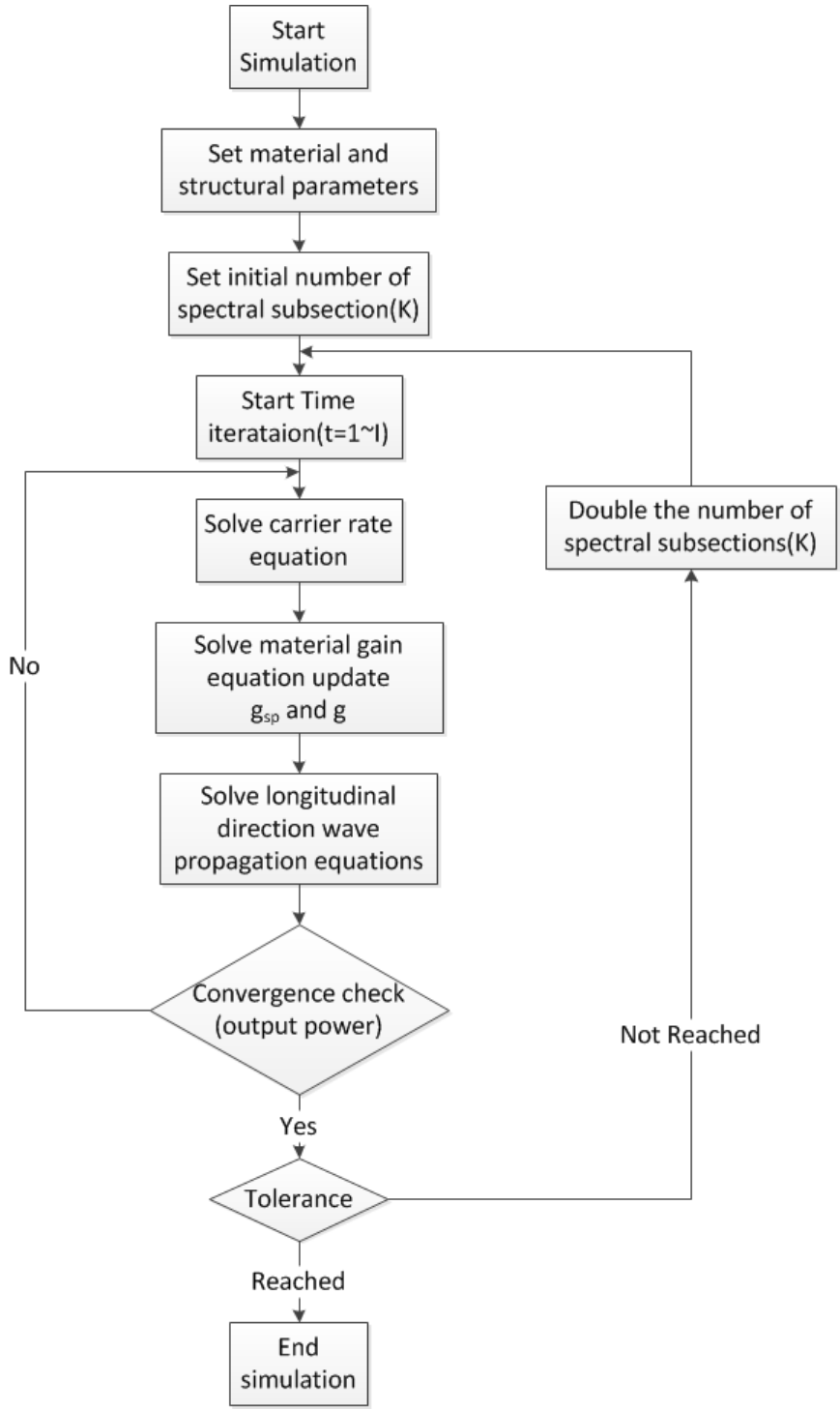

Figure 3.7: Numerical algorithm for RSOA simulation.

Firstly, a small K is selected (i.e. a few slices is divided in the ASE spectrum), the numerical simulation results obtained with the small K are stored. Secondly, double K. This is equivalent to double the number of spectral slices. The simulation results of the new discretization method are obtained and compared with the previous one. Then this iterative process continues by updating the simulation results and doubling K until a convergence is reached. The convergence is defined as no significant deviation can be found between the adjacent two simulation results. Our simulation shows that this algorithm works well and can reach a convergence quickly. Unless specified otherwise K is chosen as 40 in the following simulation.

3.6 Numerical Analysis

In looking at the device performance and the device cavity (i.e., the structure along the longitudinal direction) design problems, equation 3.18 is often used in conjunction with the optical governing equations given in section 3.2. we can work on the 2D optical field eigenvalue problem in the cross-section separately as we do in subsection 3.2.3, in order to obtain confinement factor and effective index of the structure. In device modeling, these calculations then provide the effective parameters for the longitudinal 1D equations. So we just need to handle 2D problem for optical field in the cross-section plus a 1D self-consistent problem with optical field in cross-section incorporated along the longitudinal wave propagation direction, instead of solving the full 3D problem with every aspect coupled together. This method seems to offer us an excellent balance between accuracy and efficiency in practice [Xun Li, 2009]. In our simulation, A 1550nm InGaAsP/InP RSOA with MQW active region is taken.

Normally equation 3.1 does not have analytical solution, therefore, it can only

be solved with numerical method [W.H. Press, S.A. Teukolsky, W.T. Vetterling, et al., 1992]. By using the finite difference method, as shown in figure 3.6, the total length of the SOA can be divided into N parts ($n = 1, 2, ..., N$) along wave propagation direction. Then we use forward and backward finite difference method for time mesh (denoted by i), space mesh (denoted by n) and spectral mesh (denoted by k) respectively to discretize equation 3.1 and equation 3.20 can be obtained:

$$\begin{bmatrix} e^f_{n+1,i+1,k} \\ e^r_{n-1,i+1,k} \end{bmatrix} = (1-\eta_N) \begin{bmatrix} e^f_{n+1,i,k} \\ e^r_{n-1,i,k} \end{bmatrix} + \eta_N \begin{bmatrix} 1 + A^{11}_{n,i,k}dz & A^{12}_{n,i,k}dz \\ A^{21}_{n,i,k}dz & 1 + A^{22}_{n,i,k}dz \end{bmatrix} \begin{bmatrix} e^f_{n,i,k} \\ e^r_{n,i,k} \end{bmatrix} + \eta_N dz \begin{bmatrix} s^f_{n,i,k} \\ s^r_{n,i,k} \end{bmatrix} \tag{3.20}$$

where in equation 3.20, $A^{11}_{n,i,k} = A^{22}_{n,i,k} = -j\left(\beta_k + \frac{1}{2}\Gamma_i\alpha_m g_{n,i,k}\right) + \frac{1}{2}\Gamma_i g_{n,i,k} - \frac{1}{2}\alpha_s$, $A^{12}_{n,i,k} = A^{21}_{n,i,k} = 0$. For each input signal wavelength λ_k ($k = 1, 2, ..., K$) within the range of wavelength spectrum, there is one equation like equation 3.20. So for all K wavelengths there should be a set of K equations. And all K wavelengths share the same group of carrier in the asymmetric RSOA, which is indicated in equation 3.18. So that different intensities for signals at different wavelengths will show in the computation of in equation 3.18. Boundary condition can be expressed as $e^f_{0,i,k} = E^{in}_k + r_1 e^r_{0,i,k}$, $e^r_{N,i,k} = r_2 e^f_{N,i,k}$ at left and right facet of the cavity, respectively. The carrier rate equation 3.18 can be discretized to:

$$N_{n,i+1} = N_{n,i} + \{\frac{\eta J}{eh} - \left(AN_{n,i} + BN^2_{n,i} + CN^3_{n,i}\right) - R^{stim}_{n,i}\}\Delta t \tag{3.21}$$

where $R_{n,i}^{stim}$ represents:

$$R_{n,i}^{stim} = \sum_{k=1}^{K} \frac{n_{eff_i}}{4\hbar\omega_k} \sqrt{\frac{\epsilon_0}{\mu_0}} \frac{\Gamma_i}{\sum_{ar}} g_{n,i,k} \{ |e_{n,i,k}^{f} exp(j\beta_k n\Delta z) + e_{n,i,k}^{r} exp(-j\beta_k n\Delta z)|^2 \\ + |e_{n-1,i,k}^{f} exp(j\beta_k (n-1)\Delta z) + e_{n-1,i,k}^{r} exp(-j\beta_k (n-1)\Delta z)|^2 \}, \tag{3.22}$$

In equation 3.20, $n = 1, 2, ..., N$, $i = 1, 2, ...,$ $k = 1, 2, ..., K$, $\Delta z = \eta_N v_g \Delta t$. In order to solve the discretized equations, we start from $N_{n,1} = N_{tr}$, $g_{n,1,k} = 0$, $E_{n,1,k}^{f,b} = 0$. The amplitude of spontaneous emission can be approximately modeled by the Gaussian distributed random process while the phase of the noise can be modeled by uniformly distributed random process. The Gaussian distributed random number generators should satisfy the following condition:

$$\left\langle |s_{n,i,k}^{f,r}| |s_{n',i',k'}^{*f,r}| \right\rangle = 2\sqrt{\frac{\mu_0}{\varepsilon_0}} \frac{\gamma \Gamma_i g_{sp}(n,i,k)\hbar\omega_k}{n_{eff_i}} \delta_{nn'} \delta_{ii'} \delta_{kk'}, \tag{3.23}$$

In the above equation $s_{n,i,k}^{f,r}$ is a pseudorandom sequence, $\delta_{nn'}$ $\delta_{ii'}$ $\delta_{kk'}$ are Kronecker functions. By plugging $s_{n,i,k}^{f,r}$ into equation 3.21 and E_{in} into boundary conditions, $e_{n,2,k}^{f,r}$ can be obtained. If we set $J_{n,1} = \frac{eh}{\eta}\left(AN_{n,1} + BN_{n,1}^2 + CN_{n,1}^3\right) + \delta J$, then we can calculate $N_{n,2}$ from 3.21. Utilizing $N_{n,2}$ in 3.15, $g_{n,2,k}$ can be obtained. Repeating the above steps, $e_{n,3,k}^{f,r}$, $N_{n,3}$ can be obtained, all the way to the end of the time span. The device structural and material parameters [Alan E. Willner, William Shieh, 1995, Mariano G. Cara, Lorenzo Occhi, and Salvador Balle, 2003, Michael J. Connelly, 2002] are summarized in Table 3.1 :

Symbol	Parameter	Value
c	Speed of light in vacuum	$299792458 m/s$
h	Planck's constant	$6.62606 \times 10^{-34} Js$
ε_0	Vacuum permittivity	$8.8541878176 \times 10^{-12} F/m$
μ_0	Vacuum permeability	$4\pi \times 10^{-7} H/m$
R_1	Left (anti-reflective) facet power reflectivity	0
R_2	Right (reflective) facet power reflectivity	1
d	Active region thickness	$0.1\ \mu m$
N_{tr}	Transparent carrier density	$2 \times 10^{24}\ 1/m^3$
a_m	Linewidth enhancement factor	-4
n_g	Group refractive index	3.5
η_N	Ratio between time and space sample mesh	1
α_s	Power absorption loss	$1000\ 1/m$
η	Current injection efficiency	1
γ	Spontaneous coupling coefficient	1×10^{-2}
A	Non-radiative recombination coefficient	$2 \times 10^{8}\ 1/s$
B	Spontaneous emission or bimolecular radiative recombination coefficient	$5 \times 10^{-16}\ m^3/s$
C	Auger recombination coefficient	$3.5 \times 10^{-41}\ m^6/s$

Table 3.1: Simulation parameters.

3.7 Summary

In this chapter, a quasi-2D model of asymmetric RSOA is derived and analyzed numerically. The corresponding parameters and boundary conditions in our simulation are also presented. The model, parameters and boundary conditions are utilized to obtain the simulation results in Chapter 4.

Chapter 4

Design of Asymmetric Reflective Semiconductor Optical Amplifiers

4.1 Introduction

As we discussed previously, RSOAs in optical network units (ONUs) are operated in the gain saturation region so that the amplitude squeezing effect can be used to erase the information on downstream signals, however, the upstream signals go through the same RSOA need to be amplified. Therefore, it is highly demanded to search for an alternative RSOA that has the feature of erasing the downstream signal information as well as amplifying the upstream signal. In this thesis, an asymmetric RSOA by using non-uniform ridge width is proposed. Comparing with the existing symmetric RSOAs, this device has better performance in squeezing downstream signal as well as amplifying upstream signal. This chapter starts with identification of effective factors of gain difference between upstream and downstream signals and the effects of the factors are discussed. An optimized structure is then proposed according to the

effects of the factors. The performance of the asymmetric RSOA is compared with symmetric RSOA at last.

4.2 Effective Factors of Gain Difference Between Upstream and Downstream Signals

Simulation model and parameters in Chapter 3 are utilized to obtain the following simulation results. The space sample mesh Δz is set as $2\mu m$ and time sample mesh Δt is set as $\Delta t = \eta_N \Delta z / v_g$, where v_g is the group velocity. The ASE spectrum is uniformly sliced into $K = 40$ segments. Downstream gain is defined as the ratio of the signal power at the right (reflective) facet (P_{out2} in figure 3.1) to the input signal power at the input facet (P_{in} in figure 3.1); upstream gain is defined as the ratio of the output signal power at the left (anti-reflective) facet (P_{out2} in figure 3.1) to the signal power at the right (reflective) facet (P_{out1} in figure 3.1).

Difference between Wide End and Narrow End Effective Indices

In figure 4.1, bias current is set as $200mA$, cavity length is set as $380\mu m$. Power reflectivity of left facet and right facet are set as $R_1 = 0$ and $R_2 = 1$, respectively. Narrow end effective index is 3.194. As illustrated in figure 4.1, gain difference between the upstream and downstream signal increases when the difference between effective indices at the wide end and narrow end becomes larger. Gain difference equals to zero when wide end and narrow end effective indices are the same. Therefore, in order to obtain large gain difference between upstream gain and downstream gain we should make the difference between effective indices at the wide end and narrow end as large

as possible. It is also worth mentioning that wide and narrow end effective indices are the dominant factors of the gain differences comparing with other factors. By increasing the difference between effective indices at wide end and narrow end, gain difference can vary from $0dB$ to more than $15dB$. The remaining effective factors usually can give the gain difference a variance of less than $1dB$.

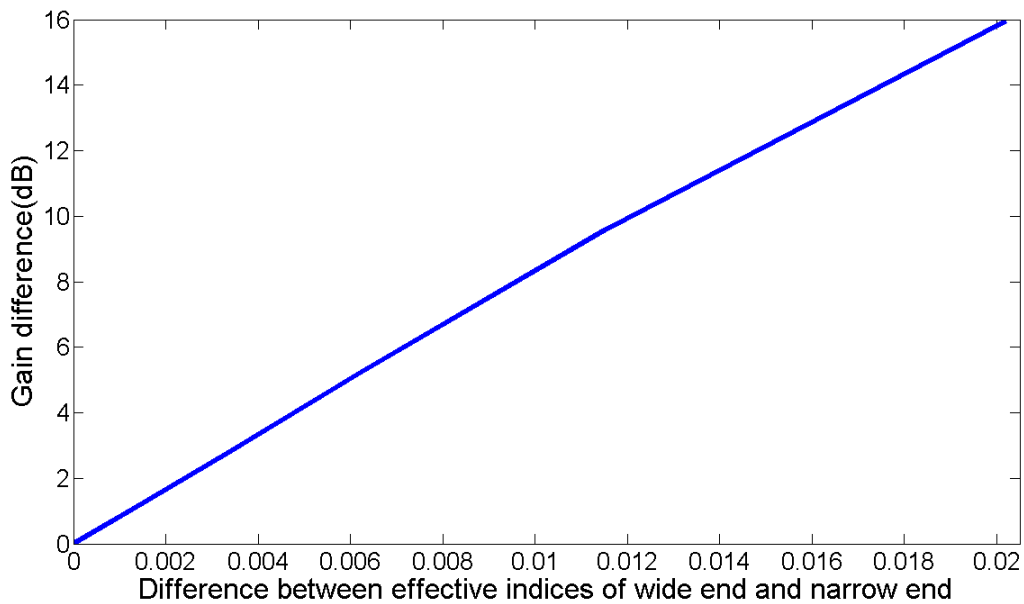

Figure 4.1: Gain difference changes with difference between wide end and narrow end effective indices.

In order to maximize the difference between effective indices at wide end and narrow end, an optimize the cross sectional structure need to be found. The illustration of the cross sectional structure is in figure 3.2. As we can see, there are several parameters in the structure that can be optimized, including the effective indices and thickness of SCH (separated confinement heterostructure) layer1 and SCH layer2;

height of the ridge, number of the wells and barrier thickness.

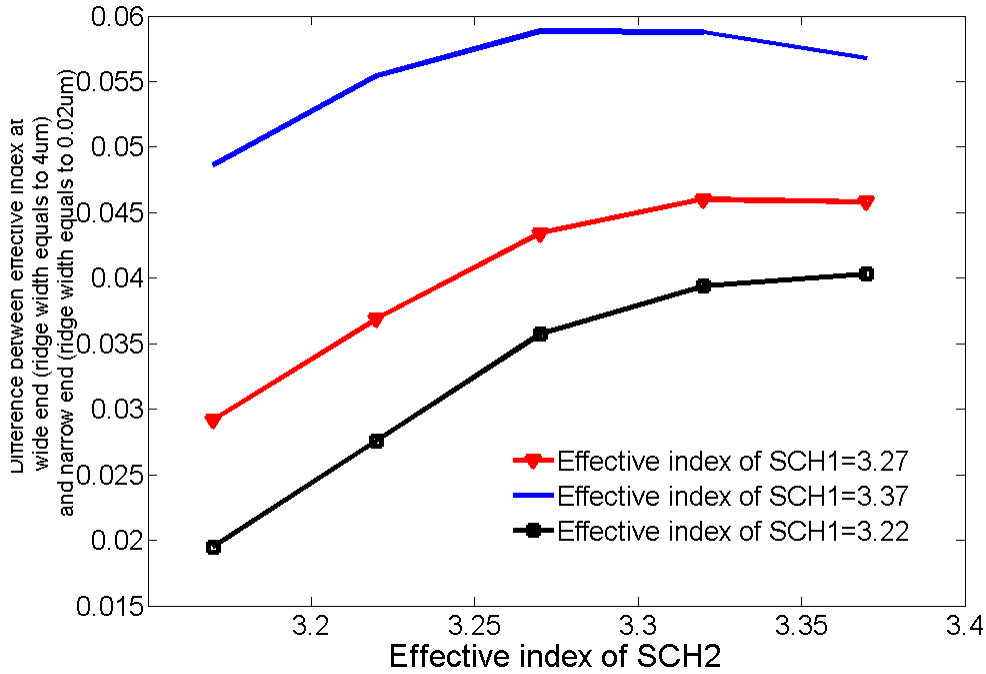

Figure 4.2: Difference between effective indices at wide and narrow end changes with effective index of SCH layer2 with different effective index of SCH layer1.

It shows that the difference between effective indices at wide and narrow end becomes larger when the effective index of the SCH layer 1 is larger. The effective index of the SCH layer 1 is no larger than the effective index of barriers. So the effective indices of SCH layer 1 and SCH layer 2 should be 3.37 and 3.27 respectively.

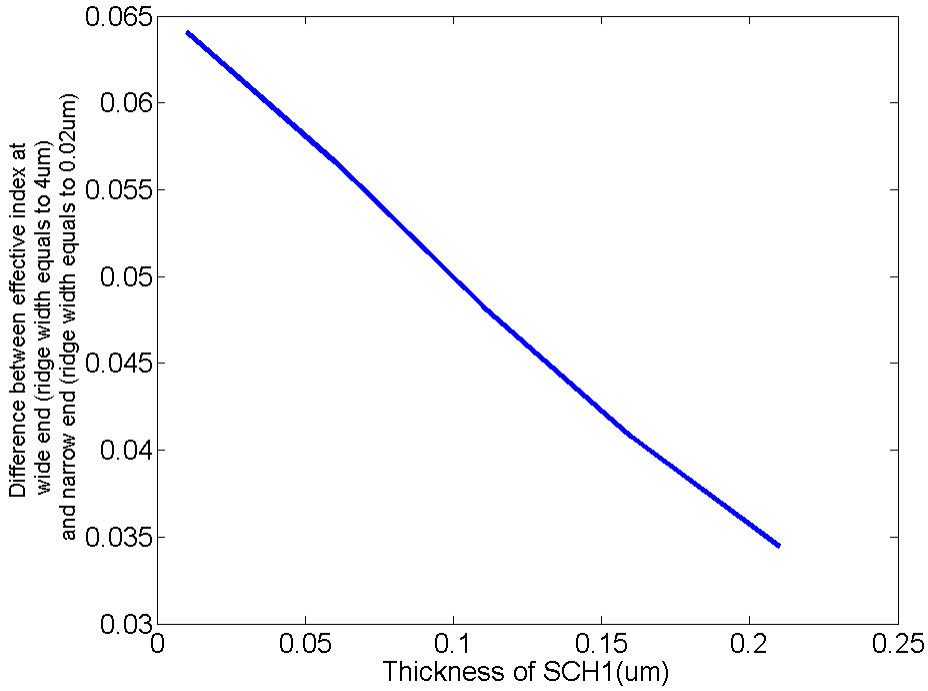

Figure 4.3: Difference between effective indices at wide and narrow end changes with thickness of SCH layer1.

With the fixed effective indices, we can adjust the thickness of SCH 1 and SCH 2 layer to obtain largest difference between effective indices at the wide and narrow ends. In figure 4.3, we can see that the difference between effective indices decreases with the increase of thickness of SCH 1 layer, largest effective index difference can be obtained when the thickness of SCH layer1 is $0.01\mu m$.

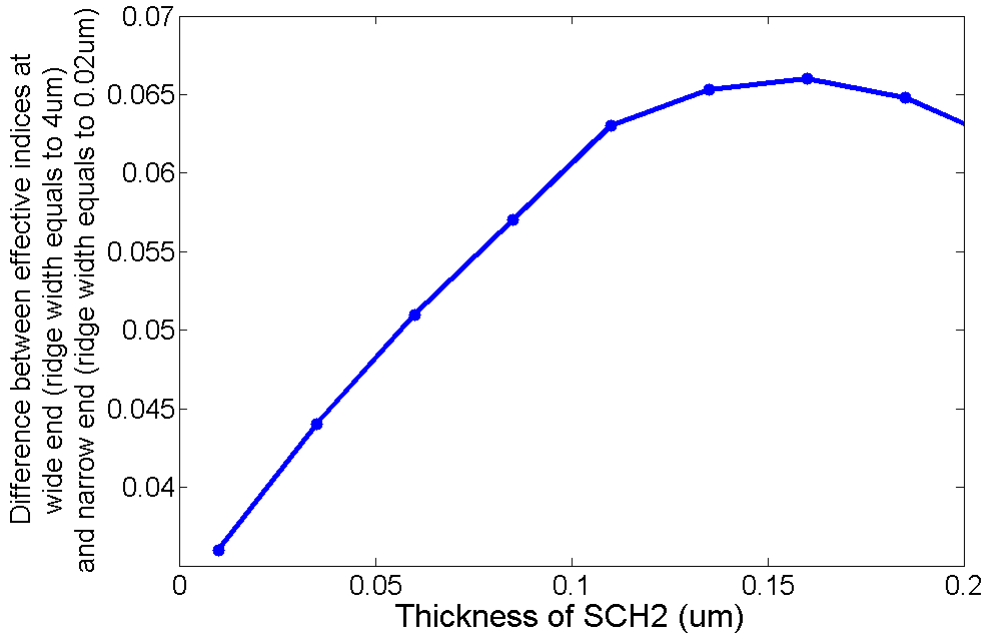

Figure 4.4: Difference between effective indices at wide and narrow end changes with thickness of SCH layer2.

Figure 4.4 illustrates how difference between effective indices at wide and narrow end changes with thickness of SCH layer2. When the thickness of SCH layer 2 equals to $0.16\mu m$, the peak value of effective index difference can be obtained.

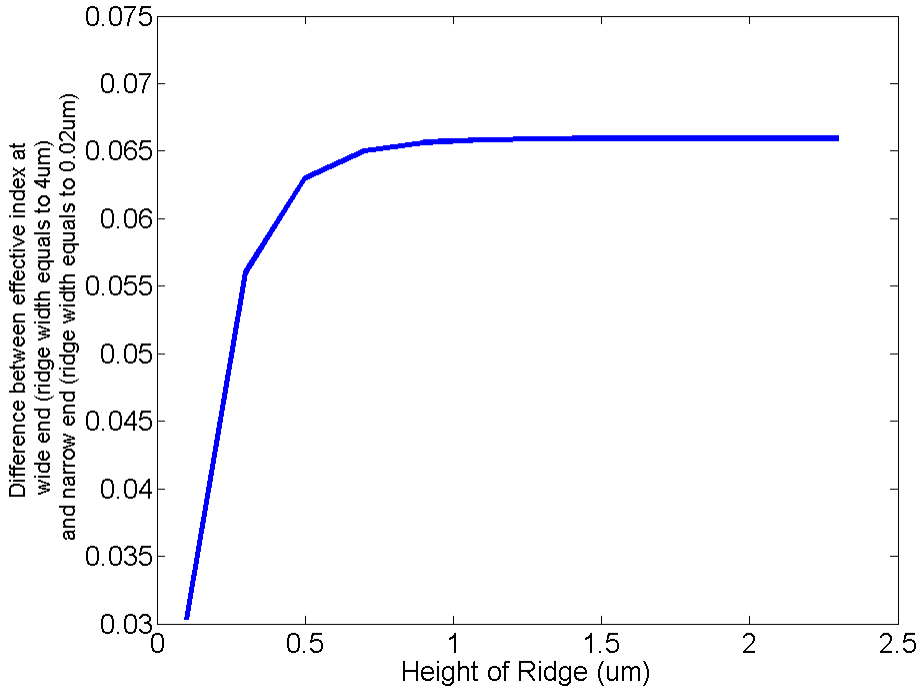

Figure 4.5: Difference between effective indices at wide and narrow end changes with ridge height.

Ridge height also has effect on difference between effective indices at wide and narrow end. When the height of ridge is smaller than $1.3\mu m$, the difference between effective indices becomes larger with the increase of height of ridge, when the height of ridge is larger than $1.3\mu m$ the difference between effective indices does not become larger with the increase of ridge height. So ridge height can be set to $1.3\mu m$.

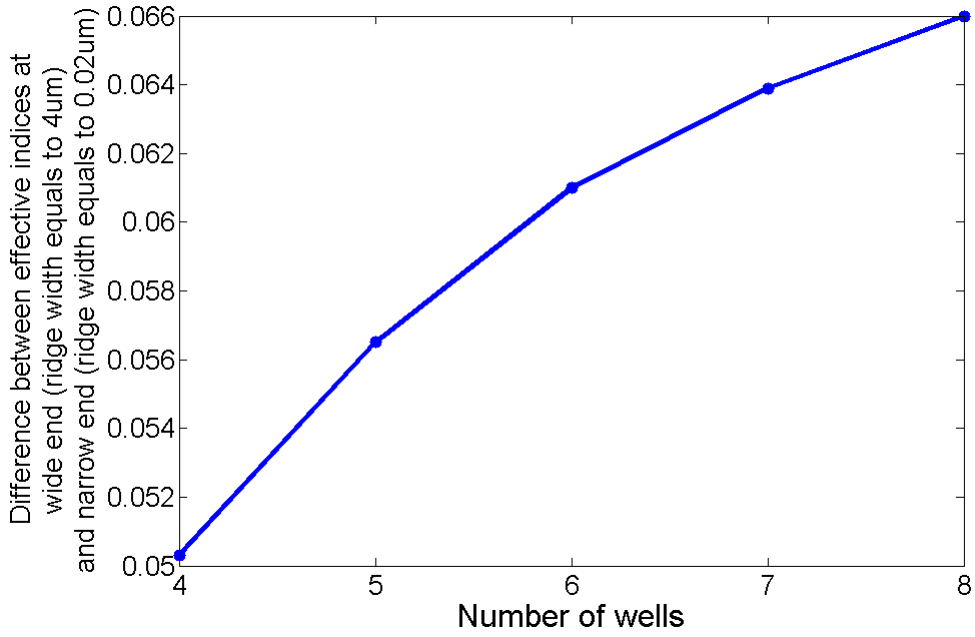

Figure 4.6: Difference between effective indices at wide and narrow end changes with number of wells.

As it shows in figure 4.6, the more the wells the larger the difference between effective indices. Barrier thickness was proven to be not influential on the difference between the effective indices, it is chosen as $8nm$ in the following simulation.

In a conclusion, the optimized cross sectional design should be the structure in figure 4.7

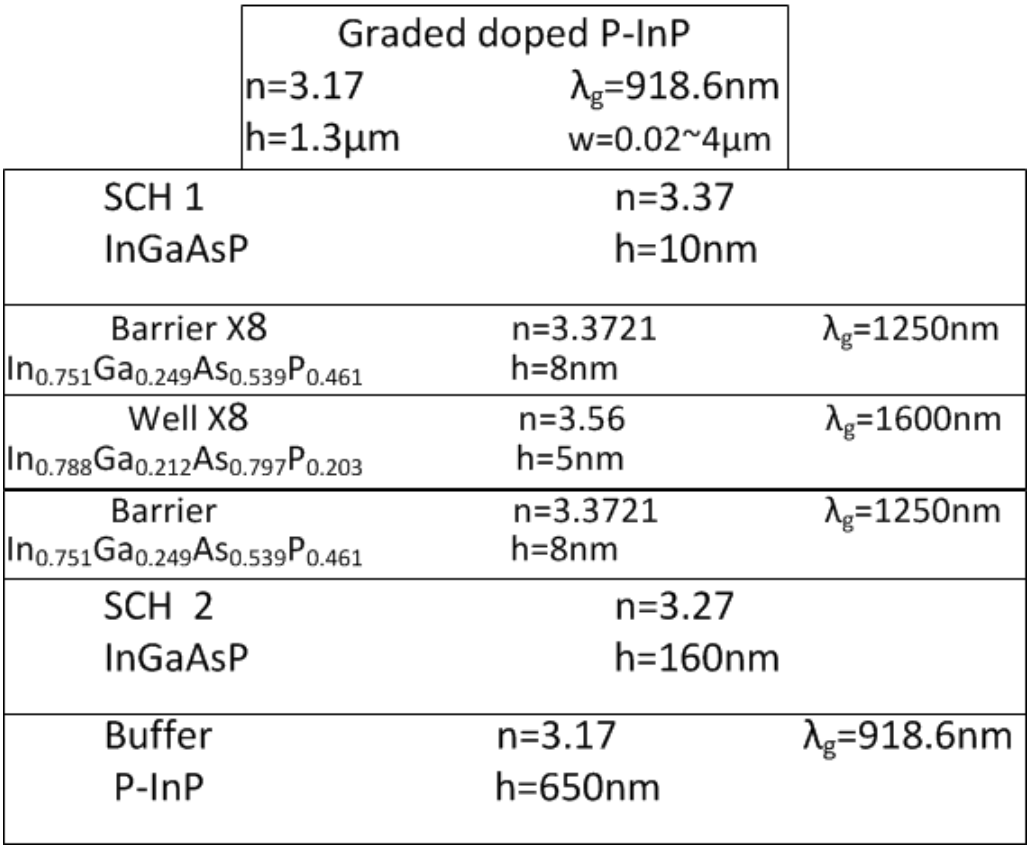

Figure 4.7: Optimized cross sectional structure.

The Way Effective index Changes From the Wide End to the Narrow End

If we use n_{wide} and n_{narrow} to denote the effective indices at the wide and narrow end respectively. The change of ridge width from n_{wide} to n_{narrow} can be described by $n(i) = n_{wide} - (n_{wide} - n_{narrow})(i/N)^{order}$, where $n(i)$ is the effective index at the $i - th$ space sample, N is the total number of space samples and *order* denotes the order of the change function.

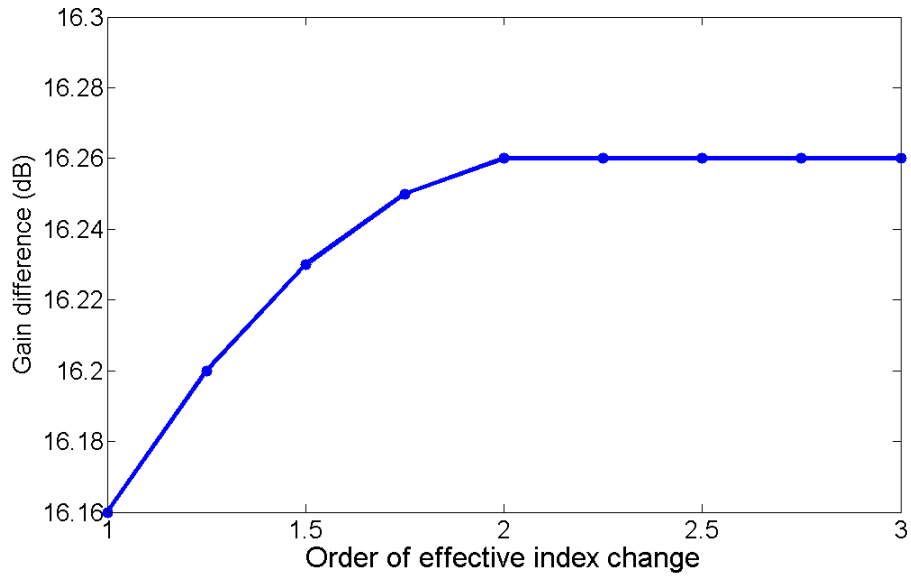

Figure 4.8: Gain difference changes with order of effective index change function.

In figure 4.8, bias current=200mA. Power reflectivity of left facet and right facet are set as $R_1 = 0$ and $R_2 = 1$, respectively. When the order of change function is equal or larger to 2, gain difference between upstream gain and downstream gain is slightly larger than the gain difference obtained in linearly changing effective index. However, the production complexity of non-linearly changing effective index is much higher, the slight increase of gain difference in the non-linearly changing effective index structure cannot possibly compensate the production difficulty it caused. So linearly changing effective index structure is chosen for simulation.

Cavity Length

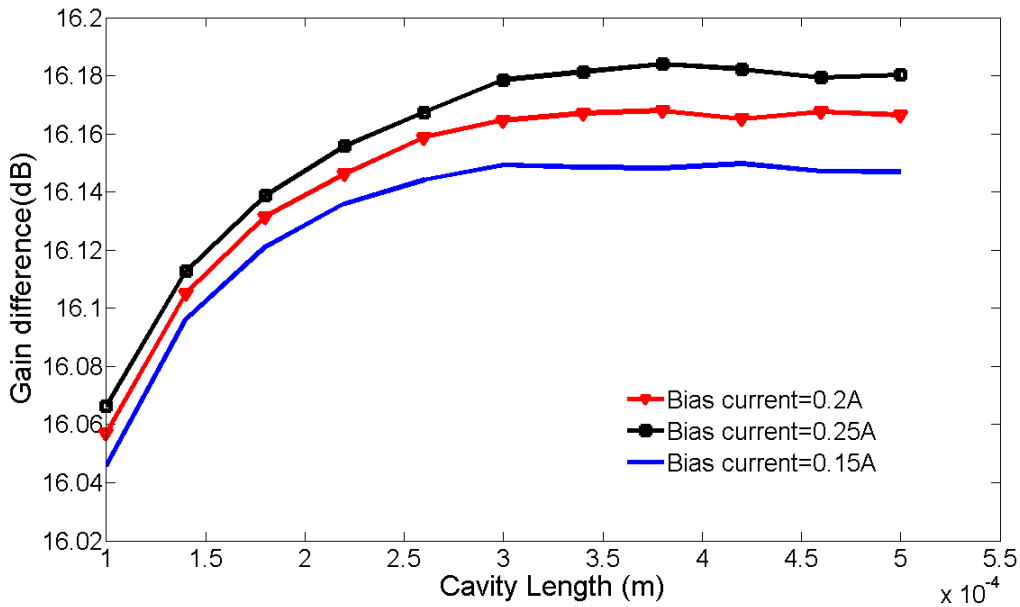

Figure 4.9: Gain difference changes with cavity length with different bias current.

In figure 4.9, power reflectivity of left facet and right facet are set as $R1 = 0$ and $R2 = 1$, respectively. Three different bias currents are injected in the asymmetric RSOA, they are $250mA$, $200mA$, $150mA$ current respectively. Comparing the three lines in the figure,we can see that with larger the bias current, larger the gain difference between upstream gain and downstream gain can be obtained.

According to the analysis above, the optimized design of RSOA should have the optimized cross-sectional structure with the cavity length of is $380\mu m$, ridge width should be changing linearly. The device has larger gain difference between upstream gain and downstream gain when it is working under larger bias current.

4.3 Performance of the Asymmetric RSOA

In figure 4.10, bias current is set as $200mA$, input wavelength is $1550nm$, extinction ratio of the input signal is 10, duty cycle is 50. As illustrated in the waveform of the signal some overshoots occur. The overshoots can be explained by the highly nonuniform distribution of the carrier density caused by the ASE [Ginovart, F., J.C. Simon and I. Valiente, 2001].

Figure 4.10(a) is input signal with 2GHz frequency. Figure 4.10(b) and figure 4.10(c) are comparison of downstream and upstream output power in the asymmetric RSOA and symmetric RSOA, respectively. Comparing the two output power profiles in figure 4.10(b) , it is noticeable that by using the asymmetric RSOA the extinction ratio is smaller than the extinction ratio of the input power and the output power of symmetric RSOA, indicating that asymmetric RSOA can erase the information in downstream signal.

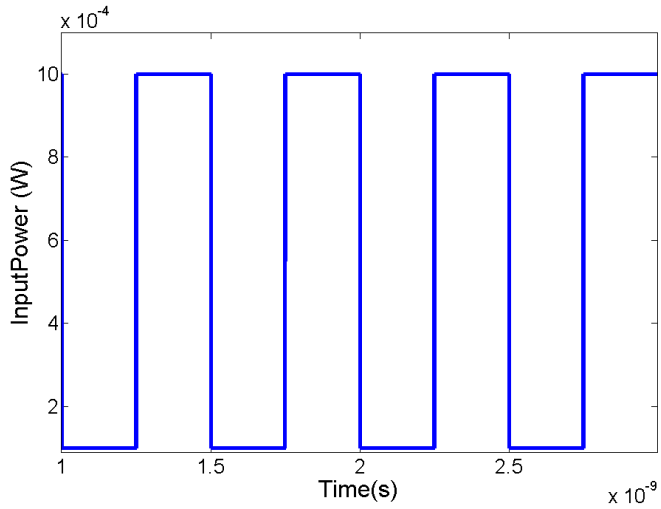
x 10^-4
10
8
6
4
2
InputPower (W)
1
1.5
2
2.5
Time(s)
x 10^-9

(a)

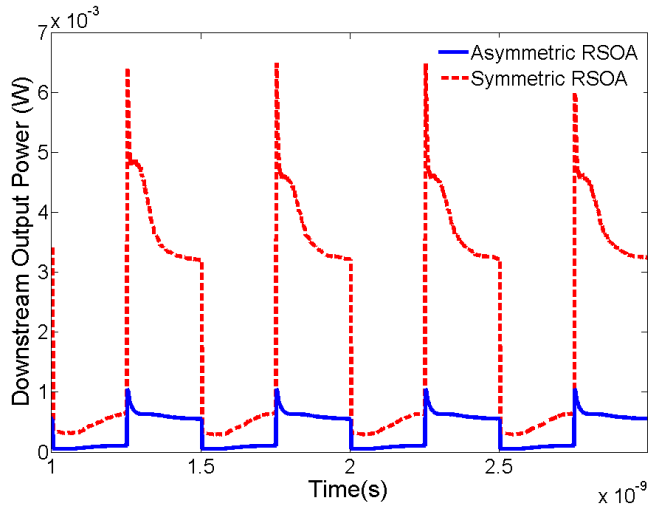
x 10^-3
7
6
5
4
3
2
1
0
Downstream Output Power (W)
Asymmetric RSOA
Symmetric RSOA
1
1.5
2
2.5
Time(s)
x 10^-9

(b)

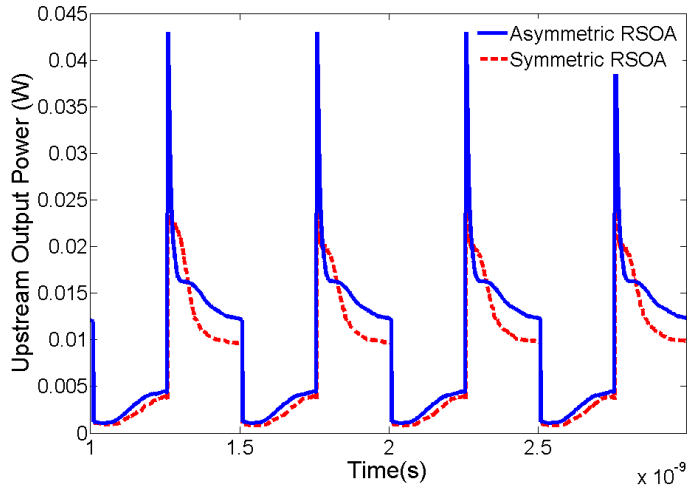

(c)

Figure 4.10: Comparison of downstream and upstream power of asymmetric RSOA and symmetric RSOA: (a) Input power from the wide (anti-reflective) end , (b) Comparison of downstream output power from the narrow (reflective) end in the asymmetric RSOA and symmetric RSOA, (c) Comparison of upstream output power from the wide (anti-reflective) end in the asymmetric RSOA and symmetric RSOA.

Comparing the output power profiles in figure 4.10, we can see that the input power is strongly squeezed in asymmetric RSOA. The downstream signal power (i.e. the reflected power) in asymmetric RSOA is much smaller than that in the symmetric RSOA, however, with the strong upstream amplifying ability, the upstream output power of asymmetric RSOA is larger than the upstream output power of symmetric RSOA. The asymmetric RSOA, comparing with symmetric RSOA, has better performance in erasing the information of the downstream signal as well as amplifying the upstream signal.

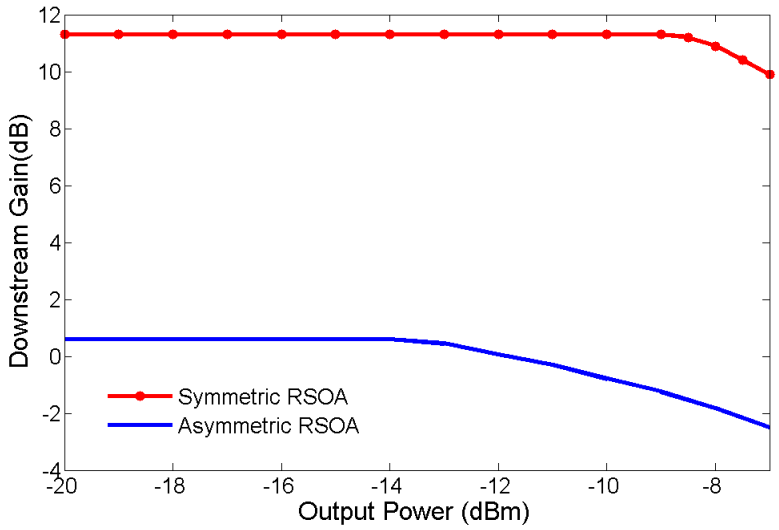

Figure 4.11: Downstream gain changes with output power from the narrow end.

Figure 4.11 shows the dependence of downstream gain on output power in symmetric RSOA(constant ridge width equals to the wide end ridge width of the asymmetric RSOA, $r_1 = 0$, $r_2 = 1$) and asymmetric RSOA, respectively. Comparing the two profiles, we can obtained the conclusion that the saturation output power of asymmetric RSOA is lower than that of symmetric RSOA and the unsaturated downstream gain of asymmetric RSOA is lower than unsaturated downstream gain of symmetric RSOA. Asymmetric RSOA is more effective in the application of erasing the information on downstream signal.

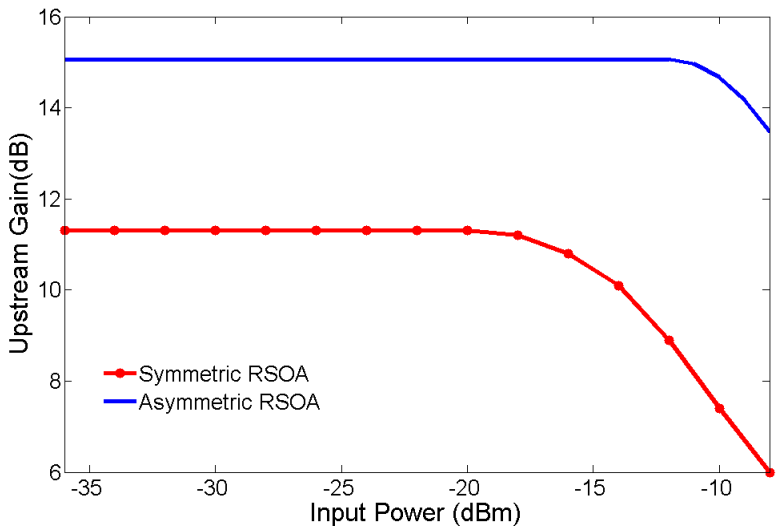

Figure 4.12: Upstream gain changes with input power.

Figure 4.12 shows the dependence of upstream gain on input power of asymmetric RSOA and symmetric RSOA respectively. Comparing the two lines in the figure, we can obtained the conclusion that the upstream gain of asymmetric RSOA is larger than that of a regular RSOA, i.e. asymmetric RSOA has better function in amplifying upstream signal.

4.4 Summary

In this chapter, we have proposed a new design for RSOA in ONU by using asymmetric ridge width. Four effective factors were studied. How the device performance is affected by the factors were analyzed. An optimized structure is then proposed according to the effects of the factors. The performance of the asymmetric RSOA is compared with symmetric RSOA. The asymmetric RSOA shows better performance

in erasing the downstream signal information as well as amplifying upstream signal.

Chapter 5

Conclusions and Future Work

5.1 Summary of Work

In this thesis, an asymmetric RSOA design is proposed and demonstrated. The ridge width becomes narrower along the traveling direction of the downstream signal so that the downstream signal can be amplified in the saturation region of the asymmetric RSOA, at the same time, the ridge width increases in the traveling direction of the upstream signal,thus the modulated upstream signal can be amplified by the asymmetric RSOA. In this thesis, I mainly focus on the designing of the structure of the asymmetric RSOA to enlarge the gain difference between upstream and downstream gain. Difference between wide end effective index and narrow end effective index, cavity length, the way effective index changes from the wide end to the narrow end and bias current are factors that can affect the gain difference. Their effects on gain difference between upstream and downstream gain are studied and demonstrated in this thesis. The performance of the asymmetric RSOA is studied and compared with symmetric RSOA. The asymmetric RSOA shows better performance in erasing

the downstream signal information as well as amplifying upstream signal.

5.2 Suggestions for Future Research

Based on the research work done in this thesis, following topics are worth further study:

1. In Chapter 3, material gain, effective index and confinement are considered separately by solving 2D optical field eigenvalue problem in the cross-sectional area. In device modeling, these calculations then provide the effective parameters for the longitudinal 1D equations. The same procedures can be done on solving carrier so that the simulation model can be more accurate and therefore provide more exact results.

2. In Chapter 4, the effects of difference between wide end effective index and narrow end effective index, cavity length, the way effective index changes from the wide end to the narrow end and bias current on gain difference between upstream and downstream gain are studied and according to their effect a comparatively best structure was obtained. Other optimize methods may be applied on obtaining an optimized structure.

Bibliography

A. Yariv (1988). Scaling laws and minimum threshold currents for quantum-confined semiconductor lasers. *Applied Physics Letters*, **53**, 1033–1035.

Alan E. Willner, William Shieh (1995). Optimal Spectral and Power Parameters for All-Optical Wavelength Shifting: Single Stage, Fanout, and Cascadability. *IEEE Journal of Lightwave Technology*, **13**, 771–781.

Alexei Sadovnikov, Xun Li, Wei-Ping Huang (1995). A Two-Dimensional DFB Laser Model Accounting for Carrier Transport Effects. *IEEE J. Quantum Electron.*, **31**, 1856 – 1862.

Amitabha Banerjee,Youngil Park, et al. (2005). Wavelength-division-multiplexed passive optical network (WDM-PON) technologies for broadband access: a review . *Journal of Optical Networking*, **4**, 737–758.

Arman B.Fallahkhair, Kai.S.Li, Thomas E.Murphy (2008). Vector Finite Difference Modesolver for Anisotropic Dielectric Waveguides. *IEEE J. Lightwave Technol.*, **26**, 1423–1431.

C. F. Janz and J. N. McMullin (1995). Spontaneous emission coupling to radiation and guided modes of planar waveguides structures. *IEEE Journal of Quantum Electron*, **31**, 1344–1353.

C. H. Henry (1986). Phase noise in semiconductor lasers. *IEEE/OSA Journal of Lightwave Technology*, **4**, 298–311.

D. J. Shin, D. K. Jung, et al. (2003). 155 Mbit/s transmission using ASE-injection FabryPerot laser diode in WDM-PON over 70 C temperature range. *Electronic Letters*, **39**, 1331–1332.

Dayan Ban and Edward H. Sargent (2000). Influence of Nonuniform Carrier Distribution on the Polarization Dependence of Modal Gain in Multiquantum-Well Lasers and Semiconductor Optical Amplifiers. *IEEE Journal of Quantum Electron*, **36**, 1081–1188.

E. Wong (2012). Next-Generation Broadband Access Networks and Technologies. *IEEE J. Lightwave Technol.*, **30**, 597–608.

E. Wong, K. Lee, and T. B. Anderson (2007). Directly modulated selfseeding reflective semiconductor optical amplifiers as colorless transmitters in wavelength division multiplexed passive optical networks. *Journal of Lightwave Technology*, **25**, 67–74.

G. P. Agrawal and N. K. Dutt (1993). *Semiconductor Lasers*. Van Nostrand Reinhold, New York.

Ginovart, F., J.C. Simon and I. Valiente (2001). Gain recovery dynamics in semiconductor optical amplifier. *Optics Communications*, **199**, 111–115.

H. Kim (2011). 10-Gbps upstream transmission for WDM-PON using RSOA and delay interferometer. In *Proc. Opt. Fiber Commun. Conf. Nat. Fiber Optic Eng. Conf.*, page OMP8.

Hiroki Takesue, Toshihiko Sugie (2002). Data rewrite of wavelength channel using saturated SOA modulator for WDM metro/access networks with centralized light sources. In *Optical Communication, ECOC*.

Hiroki Takesue, Toshihiko Sugie (2003). Wavelength Channel Data Rewrite Using Saturated SOA Modulator for WDM Networks With Centralized Light Sources. *IEEE J. Lightwave technol.*, **21**, 2546–2556.

J. Piprek, J. K.White, and A. J. SpringThorpe (2002). What limits the maximum output power of long-wavelength AlGaInAs/InP laser diode. *IEEE Journal of Quantum Electron*, **38**, 1253–1259.

J Prat, PE Balaguer, JM Gene, O Diaz, S Figuerola (2002). *Fiber-to-the-Home Technologies*. Kluwer Academic Pub.

J. W. Park (2004). *Modeling simulation and performance optimization of wideband semiconductor optical amplifiers*. Ph.D. thesis, McMaster University.

J.W. Park, X. Li and W.P. Huang (2003). Performance simulation and design optimization of gain-clamped semiconductor optical amplifiers based on distributed Bragg reflectors. *IEEE Journal of Quantum Electronics*, **39**, 1415–1423.

K. Vahala and A. Yariv (1983a). Semiclassical theory of noise in semiconductor lasers: Part I. *IEEE Journal of Quantum Electron*, **19**, 1096–1101.

K. Vahala and A. Yariv (1983b). Semiclassical theory of noise in semiconductor lasers: Part II. *IEEE Journal of Quantum Electron*, **19**, 1102–1109.

K. Y. Cho, Y. Takushima, and Y. C. Chung (2010a). Colorless 10 Gbps extended reach WDM PON with low BW RSOA using MLSE. In *Proc. Opt. Fiber Commun. Conf. Nat. Fiber Optic Eng. Conf.*, page OMG2.

K. Y. Cho, Y. Takushima, and Y. C. Chung (2010b). Demonstration of 11-Gbps, 20-km reach WDM PON using directly-modulated RSOA with 4-mary PAM signal. In *Proc. Opt. Fiber Commun. Conf. Nat. Fiber Optic Eng. Conf.*, page OMG1.

K. Y. Cho, Y. Takushima, and Y. C. Chung (2010c). RSOA-based 10G WDM PON using FEC and MLSE equalizers. In *Proc. Opt. Fiber Commun. Conf. Nat. Fiber Optic Eng. Conf.*, page OMG3.

KIM, H.D., KANG, S.-G., and LEE, C.-H. (2000). A low-cost WDM source with an ASE injected Fabry-Perot semiconductor laser. *IEEE Photonics Technology Letter*, **12**, 1067–1069.

K.Y.Cho, Y.Takushima, Y.C.Chung (2008). 10-Gb/s Operation of RSOA for WDM PON. *IEEE Photonics Technology Letters*, **20**, 1533 – 1535.

L. C. Chiu and A. Yariv (1985). Quantum well lasers. *Journal of Luminescence*, **30**, 551–561.

Lirong Huang, Wei Hong and Guiying Jiang (2013). All-optical equalization based on a two-secion reflective semiconductor optical amplifier. *Optics Express*, **21**, 4598–4611.

M. D. Feuer, J. M.Wiesenfeld,et al. (1996). Single-port laser-amplifier modulators for local access. *IEEE Photonics Technology Letters*, **8**, 1175–1177.

M. J. Connelly (2001). Wideband Semiconductor Optical Amplifier Steady-State Numerical Mode. *IEEE J. Quantum Electron.*, **37**, 439–447.

M. Omella,V. Polo, et al. (2008). 10 Gbps RSOA transmission by direct duobinary modulation. In *Proc. Eur. Conf. Opt. Commun.*

M. Presi and E. Ciaramella (2011). Stable self-seeding RSOAs for WDMPONs. In *Proc. Opt. Fiber Commun. Conf. Nat. Fiber Optic Eng. Conf.*

Mariano G. Cara, Lorenzo Occhi, and Salvador Balle (2003). Modeling and Measurement of the Wavelength-Dependent Output Properties of Quantum-Well Optical Amplifiers: Effects of a Carrier-Dependent Escape Time. *IEEE Journal of Selected Topics in Quantum Electronics*, **9**, 783–787.

Mehdi Asghari, Ian H. White and Richard V. Penty (1997). Wavelength Conversion Using Semiconductor Optical Amplifiers. *IEEE Journal of Lightwave Technology*, **15**, 1181–1190.

Michael J. Connelly (2002). *Semiconductor Optical Amplifiers.* Kluwer Academic Publishers, Dordrecht.

M.S Stern (1995). Finite Difference Analysis of Planar Optical Waveguides. *Progress In Electromagnetics Research*, **10**, 123–186.

M.Yamada (1994). *Advanced theory of semiconductor lasers. In Handbook of Semiconductor Lasers and Photonic Integrated Circuits, ed.* Chapman and Hall, London.

N. Holonyak, Jr., R. M. Kolbas, R. D. Dupuis, and P. D. Dapkus (1980). Quantum-well heterostructure lasers. *IEEE Journal of Quantum Electron*, **16**, 170–186.

P. Healey, P. Townsend, C. Ford, L. Johnston, P. Townley, I. Lealman, L. Rivers, S. Perrin and R. Moore (2001). Spectral slicing WDM-PON using wavelength-seeded reflective SOAs. *Electronics Letters*, **37**, 1181–1182.

S. L. Chuang (1995). *Physics of Optoelectronic Devices*. John Wiley and Sons, Inc., New York.

Scott B. Kuntze (2009). *Controlling Semiconductor Optical Amplifiers for Robust Integrated Photonic Signal Processing*. Ph.D. thesis, University of Toronto.

T. L. Paoli (1977). Waveguiding in a strip-geometry junction laser. *IEEE Journal of Quantum Electron*, **13**, 662–668.

W. Streifer, D. R. S. and Burnham, R. D. (1978). Analysis of gain-induced waveguiding in stripe geometry diode lasers. *IEEE Journal of Quantum Electron*, **14**, 418–427.

W.H. Press, S.A. Teukolsky, W.T. Vetterling, et al. (1992). *Numerical Recipes in Fortran: The Art of Scientific Computing*. Cambridge University Press, Cambridge.

Xun Li (2009). *Optoelectronic Devices*. Cambridge University Press, Cambridge.

Y. Katagiri, K. Suzuki, and K. Aidai (1999). Intensity stabilisation of spectrum-sliced Gaussian radiation based on amplitude squeezing using semiconductor optical amplifiers with gain saturation. *Electronic Letters*, **35**, 1362–1364.

Y.-L. Hsueh, M. S. Rogge, S. Yamamoto, and L. G. Kazovsky (2005). A highly flexible and efficient passive optical network employing dynamic wavelength allocation. *IEEE Journal of Lightwave Technology*, **23**, 277–286.